1  **Reduction of protein disulfide isomerase results in open conformations and**
2  **stimulates dynamic exchange between structural ensembles**

3  Mathivanan Chinnaraj[1], Robert Flaumenhaft[2] and Nicola Pozzi[1,*]

4

5  *[1]Edward A. Doisy Department of Biochemistry and Molecular Biology, Saint Louis*
6  *University School of Medicine, St. Louis, MO, 63104, USA.*
7  *[2]Division of Hemostasis and Thrombosis, Department of Medicine, Beth Israel*
8  *Deaconess Medical Center, Harvard Medical School, Boston, Massachusetts 02115,*
9  *USA.*

10

11

12

13

14  *Corresponding authors:

15

16  Nicola Pozzi
17  Email: nicola.pozzi@health.slu.edu
18  Phone: +1-314-977-9241

19

20  Robert Flaumenhaft
21  Email: rflaumen@bidmc.harvard.edu
22  Phone: +1-617-735-4005

23

24

25  **Short title:** Protein disulfide isomerase allostery

26

27

28  **Keywords:** single-molecule FRET, protein dynamics, thiol-oxidoreductases, allostery,
29  protein disulfide isomerase, thrombosis

1    **Abstract**

2    Protein disulfide isomerase (PDI) is a ubiquitous redox-regulated enzyme that interacts
3    with hundreds of client proteins intracellularly and extracellularly. It comprises two redox-
4    sensitive domains, each hosting the conserved catalytic motif CxxC, two redox-insensitive
5    protein-binding domains, and three linkers. Snapshots of oxidized and reduced PDI have
6    been obtained by X-ray crystallography. Yet, how PDI's structure dynamically changes in
7    response to the redox microenvironment and ligand binding remain unknown. Here, we
8    used multiparameter confocal single-molecule Förster resonance energy transfer
9    (smFRET) and multiple FRET pairs to track the movements of the two catalytic domains
10   with high temporal resolution. Our studies document that, at equilibrium, PDI visits three
11   structurally distinct conformational ensembles, two "open" ($O_1$ and $O_2$) and one "closed"
12   (C). We show that the redox environment dictates the time spent in each ensemble and
13   the rate at which they exchange. While oxidized PDI samples $O_1$, $O_2$ and C more evenly
14   and in a slower fashion, reduced PDI predominantly populates $O_1$ and $O_2$, and exchanges
15   between them more rapidly, on the sub-millisecond timescale. These findings were not
16   expected based on crystallographic data. Using mutational analyses, we further
17   demonstrate that the two active sites are structurally nonequivalent and that ligands
18   targeting the active sites of reduced PDI shift the equilibrium towards closed
19   conformations of the enzyme. This work introduces a new structural framework that
20   challenges current views of PDI dynamics, helps rationalize the multifaced role of PDI in
21   biology and may assist drug development.

**Introduction**

Protein disulfide isomerase (PDI) is an archetypal oxidoreductase responsible for oxidative protein folding in eukaryotes (*1, 2*). It interacts with hundreds of client proteins catalyzing the formation, rupture, and isomerization of disulfide bonds (*1, 3*). Since disulfide bonds are essential for achieving tertiary and quaternary structures of proteins but also have important functional roles, its enzymatic activity is essential for life.

PDI comprises 508 amino acids organized in four thioredoxin domains arranged in the order **a**, **b**, **b'** and **a'**, followed by an acidic C-terminal tail **(Figure 1A)** (*1, 3*). Domains **a** (res 18-133) and **a'** (res 137-232) contain the conserved catalytic motif CxxC, whereas the **b** (res 235-348) and **b'** (res 370-479) domains are redox-insensitive; they participate in substrate and cofactor recruitment, not in catalysis. Three linkers connect the four thioredoxin domains.

While mostly located in the endoplasmic reticulum (ER) (*1*), PDI can also be found outside the cells, where it plays key regulatory roles in several enzymatic cascades, most notably in the coagulation cascade (*4-6*). However, in contrast to intracellular PDI, which primarily works as a foldase (*1, 7*), extracellular PDI mostly works as a reductase or oxidase (*4, 8*). That is, PDI facilitates the rupture or formation of specific types of disulfide bonds in target proteins, known as allosteric disulfide bonds (*9*), thus modulating their function by inducing local or global structural rearrangements. Relevant examples of allosteric disulfide bonds regulated by PDI are the ones in the coagulation activator tissue factor (*10*), in the Antiphospholipid Syndrome autoantigen $\beta_2$GPI (*11*), and in the membrane receptors αIIbβ3 (*12*) and GpIbα (*13*), which control platelet activation and aggregability.

Because of the motif CxxC, the catalytic activity of PDI is critically regulated by the microenvironment via cysteine modifications, i.e., oxidation (S-S) or reduction (- SH) (*1*). In the ER, there are several systems controlling the redox balance so that PDI is mostly oxidized (*14*). However, in the circulation, such systems are not readily available. Consequently, PDI's redox state can vary quite significantly. Hence, understanding how the structure of PDI responds to changes in the redox milieu is particularly important for the field of thrombosis and hemostasis as this knowledge could help to define the mechanistic basis of its extracellular function as well as to design compounds capable of targeting redox-specific activities of extracellular PDI for safe anticoagulation.

Over the past two decades, structural, computational, and biophysical studies have provided solid evidence for PDI's flexibility by documenting large-scale redox-dependent and redox-independent movements of the two catalytic domains (*15-21*). This led to the hypothesis that PDI operates as a dynamic clamp, which is capable of opening and closing in response to different stimuli. Testing this structure-based hypothesis, however, has been challenging due to several technical limitations. Ensemble methods, although easily accessible, are difficult to interpret on a structural basis since the signal is averaged over multiple conformations, preventing direct identification of distinct functional states.

1   Multidimensional NMR experiments are greatly complicated by the relatively large size of
2   PDI. Finally, X-ray crystallography and cryo-electron microscopy, while providing very
3   detailed information, offer a limited number of structural snapshots. X-ray crystallography
4   may also impose constraints on structural variability.
5       Recently, pioneering single-molecule studies of PDI have started to emerge in the
6   literature. Most notably, Okumura et al. applied High-Speed Atomic Force Microscopy
7   (HS-AFM) to study PDI conformational dynamics after tethering the protein onto mica
8   sheets (*20*). In the meantime, our group developed a method to incorporate unnatural
9   amino acids into PDI (*22*), thus opening the door for single-molecule Förster resonance
10  energy transfer (smFRET) investigations of PDI in solution. In this study, we provide a
11  detailed characterization of the conformational dynamics of PDI in solution using
12  multiparameter confocal smFRET. We chose this setup over other single-molecule
13  approaches, such as total internal reflection, because it enables identification and
14  quantification of large-scale dynamics with high temporal resolution (ns-ms) while
15  minimizing the probability of structural perturbations caused by immobilization of proteins
16  onto a surface (*23-25*). Our work reveals unanticipated movements of the **a** and **a'**
17  catalytic domains in response to the redox environment and ligand binding and offers a
18  new structural framework that helps rationalize the multifaced role of PDI in biology and
19  may assist drug development efforts.
20
21  **Results**
22  **Experimental design.** To perform smFRET experiments, donor and acceptor
23  fluorophores must be site-specifically introduced into the protein of interest without
24  perturbing its structure and, ideally, its biological function. Positions 57 and 88 in the **a**
25  domain and 401 and 467 in the **a'** domain were selected based on the currently available
26  X-ray structural data of oxidized **(Figure 1B, top panel)** and reduced **(Figure 1B, bottom**
27  **panel)** PDI (*16*) to obtain four combinations of labeling positions, two linear (i.e., 57/401
28  and 88/467) and two diagonal (i.e., 57/467 and 88/401). Residues K57 and K401 are
29  located one position downstream of the active site cysteines C56 and C400 in the **a** and
30  **a'** domain. Residues S88 and K467 are located on the opposite side of the catalytic
31  domains. These four FRET pairs were designed to measure large-scale hinge bending
32  movements of the **a** and **a'** domains reported by the structures and to follow the
33  positioning of the active sites relative to each other. The four FRET pairs were also
34  designed such as we expect significantly higher values of energy transfer ($\Delta_{FRET}>0.2$)
35  while transitioning from the oxidized (lower FRET) to the reduced state (higher FRET), as
36  reported in **Figure 1C**.
37
38  **Site-specific labeling of catalytically active PDI.** Given that PDI's active sites contain
39  four cysteine residues, donor (Atto550) and acceptor (Atto647N) fluorophores were
40  introduced at the desired positions using biorthogonal chemistry by following a procedure
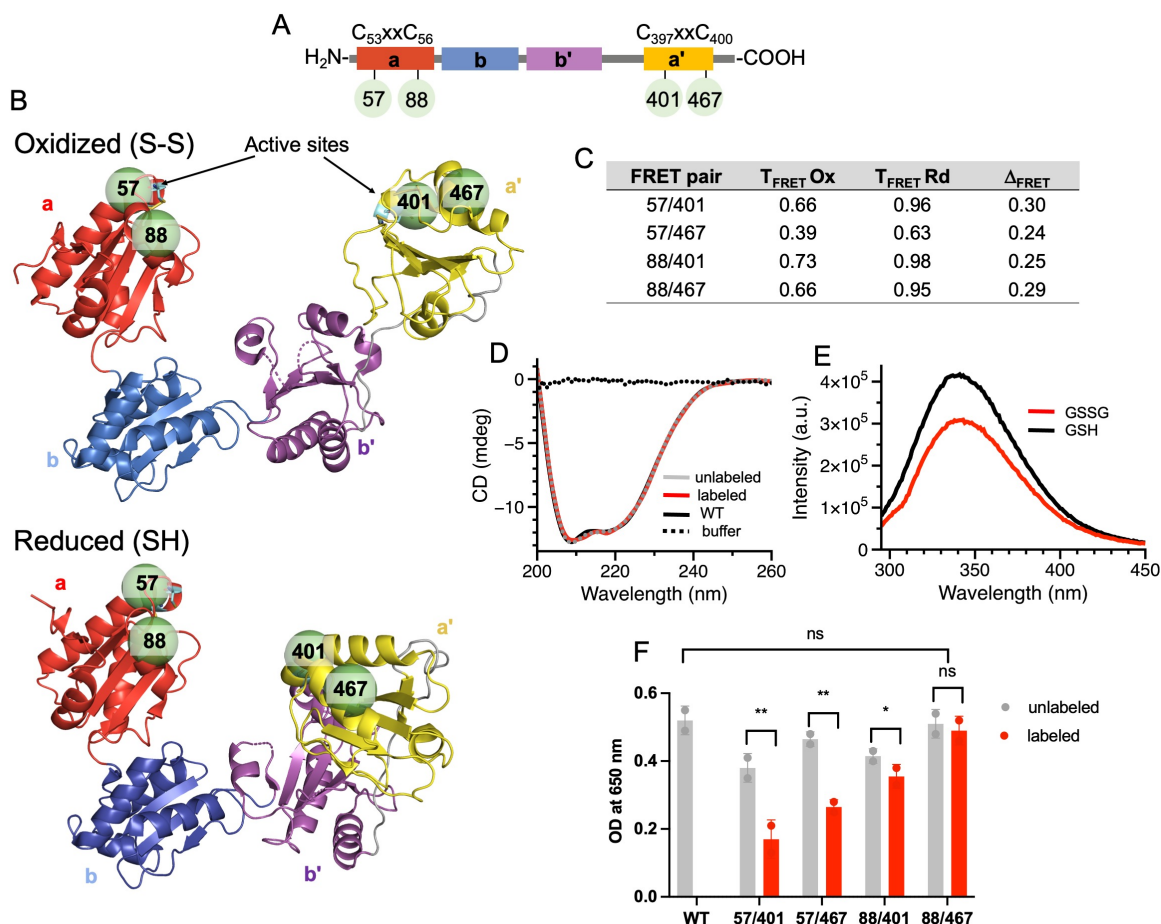
| FRET pair | $T_{FRET}$ Ox | $T_{FRET}$ Rd | $\Delta_{FRET}$ |
|-----------|---------------|---------------|-----------------|
| 57/401 | 0.66 | 0.96 | 0.30 |
| 57/467 | 0.39 | 0.63 | 0.24 |
| 88/401 | 0.73 | 0.98 | 0.25 |
| 88/467 | 0.66 | 0.95 | 0.29 |

**Figure 1. Design, structural and functional integrity of labeled proteins. A)** Domain structure of human PDI. PDI comprises 508 AA organized in four domains, **a** (red), **b** (blue), **b'** (magenta) and **a'** (yellow), connected by linkers (gray). Domains **a** and **a'** contain the active sites CxxC. **B)** Top view of the X-ray crystal structures of oxidized (S-S, top panel, 4el1) and reduced (SH, bottom panel, 4ekz) PDI documenting a U-shape architecture and movement of the **a'** domain (yellow) toward the **b'** domain (magenta) upon reduction of the active sites. Shown as dotted lines are the distances between the active sites. The green spheres represent residues K57, S88, K401 and K467 selected for smFRET studies. **C)** Theoretical values of energy transfer for oxidized ($T_{FRET}$Ox) and reduced PDI ($T_{FRET}$Rd) estimated with the software FPS after attaching Atto-550 and Atto-467N dyes ($R_0$=65Å) at the specified positions. The difference $T_{FRET}$Ox-$T_{FRET}$Rd is shown as $\Delta_{FRET}$. **D)** Far-UV CD of PDI 88/467 before (gray) and after (red) labeling compared to PDI wild-type (WT, black). **E)** Reactivity of PDI 88/467 towards oxidized (GSSG, red) and reduced (GSH, black) glutathione probed by intrinsic fluoresce spectroscopy. **F)** Insulin assay testing the reductase activity of proteins before (gray) and after (red) labeling. PDI wild type (WT) served as a control. Each reaction was continuously monitored for 60 min at 650 nm in duplicate. The intensity at 650 nm after 40 min was used as readout of catalytic efficiency. Progress curves are shown in **Figure S1. (**\*\* p<0.001), \* p<0.01, n.s. not significant).

1    recently developed and validated in our laboratory (*22*). After purification, doubly labeled

2    PDI 57/401, PDI 57/467, PDI 88/401 and 88/467 were properly folded, as documented

3    by far-UV CD **(Figure 1D** and **Figure S1)** and responded well to redox stimulation, as

4    probed by tryptophan fluorescence spectroscopy **(Figure 1E** and **Figure S1).** Similar

5    spectral variations induced by GSSG and GSH were found in previous studies for PDI

6    wild-type (*26*). Importantly, doubly labeled PDI variants remained active when tested for

1   their ability to reduce insulin to a degree consistent with what was expected based on the

2   positioning of the dyes **(Figure 1G** and **Figure S1)**. In fact, the loss of enzymatic activity

3   for doubly labeled PDI 57/401 (67%), PDI 57/467 (49%) and PDI 88/401 (32%) compared

4   to unlabeled proteins, PDI wild-type and doubly labeled PDI 88/467 was anticipated and

5   likely arises from the proximity of residue 57 and residue 401 to the active site cysteines

6   56 and 400, which interferes with substrate processing.

7      To rule out position-dependent interactions of the dyes with the protein, we measured

8   steady-state anisotropy and quantum yield for singly labeled donor and acceptor PDI

9   molecules. The values measured for the eight variants are reported in **Table 1.** They are

10   consistent with freely rotating dyes attached to PDI.

11      Taken together, these results indicate that, after purification, fluorescently labeled PDI

12   molecules are properly folded and catalytically active, thus suitable for smFRET studies.

13

14   **Conformational dynamics of oxidized and reduced PDI monitored by smFRET.**

15   smFRET studies of PDI were performed using a confocal microscope equipped with pulse

16   interleaved excitation, as detailed in the experimental section. This methodology, in

17   addition to enabling simultaneous acquisition of fluorescence intensity and fluorescence

18   lifetime, facilitates isolation and, therefore, analysis of molecules containing the proper

19   donor:acceptor ratio (stoichiometry, S=0.5) while discarding donor only (S=1) and

20   acceptor only (S=0) species, which are irrelevant for our goal **(Figure S2).** Given that $R_0$

21   of the FRET couple Atto-550/Atto-647N is ~65Å, interprobe distances from ~45Å (E=0.9)

22   to ~90Å (E=0.10) are measured in this study.

23      The 1D FRET efficiency plots of PDI 57/401, PDI 57/467, PDI 88/401 and PDI 88/467

24   obtained after size exclusion chromatography (SEC) purification, and therefore under

25   conditions in which the active site cysteines are oxidized (22), are reported in the top

26   panels of **Figure 2A, Figure 2B, Figure 2C** and **Figure 2D,** respectively. The

27   corresponding 2D plots of FRET efficiency vs Stoichiometry (S) are reported in **Figure**

28   **S3** of the supplementary materials.

29      Oxidized PDI 57/401 and PDI 88/401 were found to adopt a unimodal distribution,

30   which was skewed toward high FRET. For both variants, the mean FRET ($E_{ave,ox}$) was

31   0.82±0.16. In contrast, oxidized PDI 57/467 and PDI 88/467 displayed broader FRET

32   distributions, spanning almost the entire FRET range. This resulted in lower FRET values

33   ($E_{ave,ox}$=0.61 for PDI 57/467 and $E_{ave,ox}$=0.66 for PDI 88/467) and larger standard

34   deviations (0.24 for PDI 57/467 and 0.22 for PDI 88/467). The differences between these

35   variants are clearly visible by inspecting the plots in **Figure 2.** The values of $E_{ave,ox}$ and S

36   are summarized in **Table 2**.

37      To transform oxidized PDI into reduced PDI we added the reducing agent dithiothreitol

38   (DTT). When 1 mM DTT was added to oxidized PDI, the FRET signal shifted towards

39   lower values for all the FRET pairs (**Figure 2A, Figure 2B, Figure 2C** and **Figure 2D,**

40   **bottom panels,** and **Table 2)**. The greatest effect was seen for PDI 88/467 ($\Delta E_{ave,(ox-}$

1    rd)=0.13) followed by PDI 57/467 ($\Delta E_{ave,(ox-rd)}$=0.07). Smaller variations were measured for

2    PDI 88/401 ($\Delta E_{ave,(ox-rd)}$=0.03) and PDI 57/401 ($\Delta E_{ave,(ox-rd)}$=0.02). Moreover, PDI 57/467

3    **(Figure 2B)** and PDI 88/467 **(Figure 2D)** displayed more homogeneous distributions

4    characterized by a significantly smaller standard deviation compared to the oxidized form.

5    The changes observed in the presence of DTT were neither dye nor DTT specific since

6    similar results were obtained by labeling PDI 88/467 with a different combination of dyes

7    and by using GSH as an alternative source of reducing equivalents **(Figure S4)**.

8    Moreover, the effect of DTT on PDI 88/467 was dose-dependent and saturable, as shown

9    in **Figure 2E**. Finally, the changes induced by DTT were also consistent with our previous

10    results obtained with the FRET pair 42/467 (*22*), which reports an even more pronounced

11    high to low FRET transition in the presence of DTT ($\Delta E_{ave,(ox-rd)}$=0.31). We conclude that

12    addition of DTT triggers a profound structural reorganization forcing the catalytic domains

13    to move away from each other. Interestingly, the structural effect elicited on PDI by DTT

14    were qualitatively different from what has been previously reported for the thiol-enzyme

15    quiescin-sulfhydryl oxidase (QSOX) using smFRET (*27*), implying different sensing
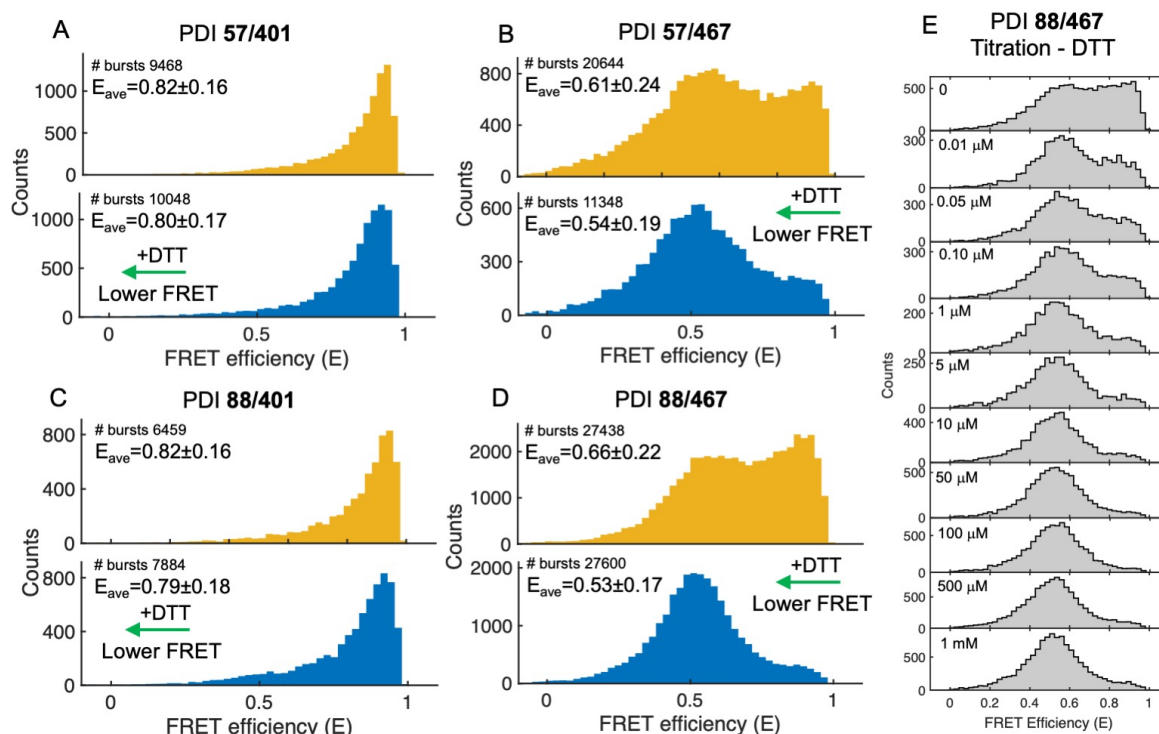
16    mechanisms between families of oxidoreductases.



**Figure 2. smFRET studies of oxidized and reduced PDI.** 1D FRET efficiency histograms of PDI 57/401 **(A)**, PDI 57/467 **(B)**, PDI 88/401 **(C)** and PDI 88/467 **(D)** obtained in the absence (yellow, top panel) and presence (cyan, bottom panel) of 1 mM DTT in Tris 20 mM pH 7.4, 150 mM NaCl, 2 mM EDTA, 0.003% Tween 20. PDI's concentration was 50-100 pM. Collection time was ~40 minutes per sample. Molecules with 0.25<S>0.75 were selected. Shown are the number of bursts and mean FRET ($E_{ave}$) ± STDEV. Note how, in the presence of DTT, the signal shifts towards lower FRET (green arrow). **(E)** 1D FRET efficiency histograms of PDI 88/467 collected at increasing concentrations of DTT (0-1 mM). To ensure equilibrium, samples were measured after incubating PDI 88/467 and DTT for 40 minutes at room temperature (20°C).

**Oxidized and reduced PDI undergo rapid conformational dynamics.** Data in **Figure 2** document significant differences between the FRET pairs. They also provide preliminary evidence that multiple conformations of oxidized PDI exist at equilibrium, and that PDI 57/467 and PDI 88/467, but not PDI 57/401 nor PDI 88/401, are capable of efficiently visualizing them when labeled with the FRET pair Atto550/647N.

By taking advantage of the way photons are collected and stored in our experiments (i.e., time-correlated single photon counting or TCSPC), we constructed 2D plots in which the transfer efficiency of oxidized and reduced PDI was graphed versus the fluorescence lifetime of the donor in the presence of the acceptor ($\tau_{D(A)}$) of each molecule. In these plots, as demonstrated elsewhere (*23-25, 28-30*), FRET populations that represent conformational states (or ensembles) that either do not exchange or exchange at a rate ~10 times slower or ~10 times faster than the molecules' diffusion time lie on the so-called "static" FRET line, which is the line that describes the theoretical relationship between the values of $\tau_{D(A)}$ and the values of energy transfer. By contrast, FRET populations that represent conformational states undergoing dynamic exchange during the observation time deviate from the "static" FRET line and lie on the "dynamic" FRET line, which connects two exchanging states. Because of the very significant effect induced by DTT **(Figure 2D)** and pristine catalytic activity **(Figure 1F)**, we selected PDI 88/467 for our in-depth biophysical analyses. However, similar considerations are applicable and remain valid for the other FRET variants, whose results are reported and briefly discussed in **Figure S5** of the supplementary materials.

For both oxidized **(Figure 3A)** and reduced PDI 88/467 **(Figure 3B),** we observed two main populations of molecules, connected by a bridge. These two populations were characterized by fluorescence lifetime values centered at ~0.25 ns and ~1.59 ns, corresponding to high-FRET and medium-FRET. For simplicity, we called these two populations closed and open, respectively.

In contrast to the closed population, the center of the open population did not reside on the static FRET line but was instead slightly shifted toward the right. This was particularly evident for oxidized PDI 88/467. Since the dyes are freely rotating in solution thus not theoretically affecting protein dynamics, we hypothesized that, in addition to C, PDI visits multiple FRET states within the open ensemble that exchange in the millisecond timescale. This is because PDI molecules remain, on average, ~0.5 ms in the observation volume.

To test this hypothesis, we performed subpopulation specific fluorescence lifetime analysis, a methodology that has proven useful to define the number of species at equilibrium that are faster than diffusion (*23, 25, 31*). Since we hypothesized heterogeneity within the open ensemble, we selected bursts from the FRET interval 0.4-0.6, which is highlighted in magenta. If multiple PDI species were present at equilibrium, we expected more than one relaxation would be necessary to fit the lifetime plots. For both oxidized and reduced PDI 88/467 **(Figure 3C** and **Table 3)**, the lifetime decay could

1    not be fit with one exponential (1 exp, $\chi^2$=9.69) but instead required a double exponential

2    function (2 exp, $\chi^2$=1.31). The addition of a third relaxation did not significantly improve

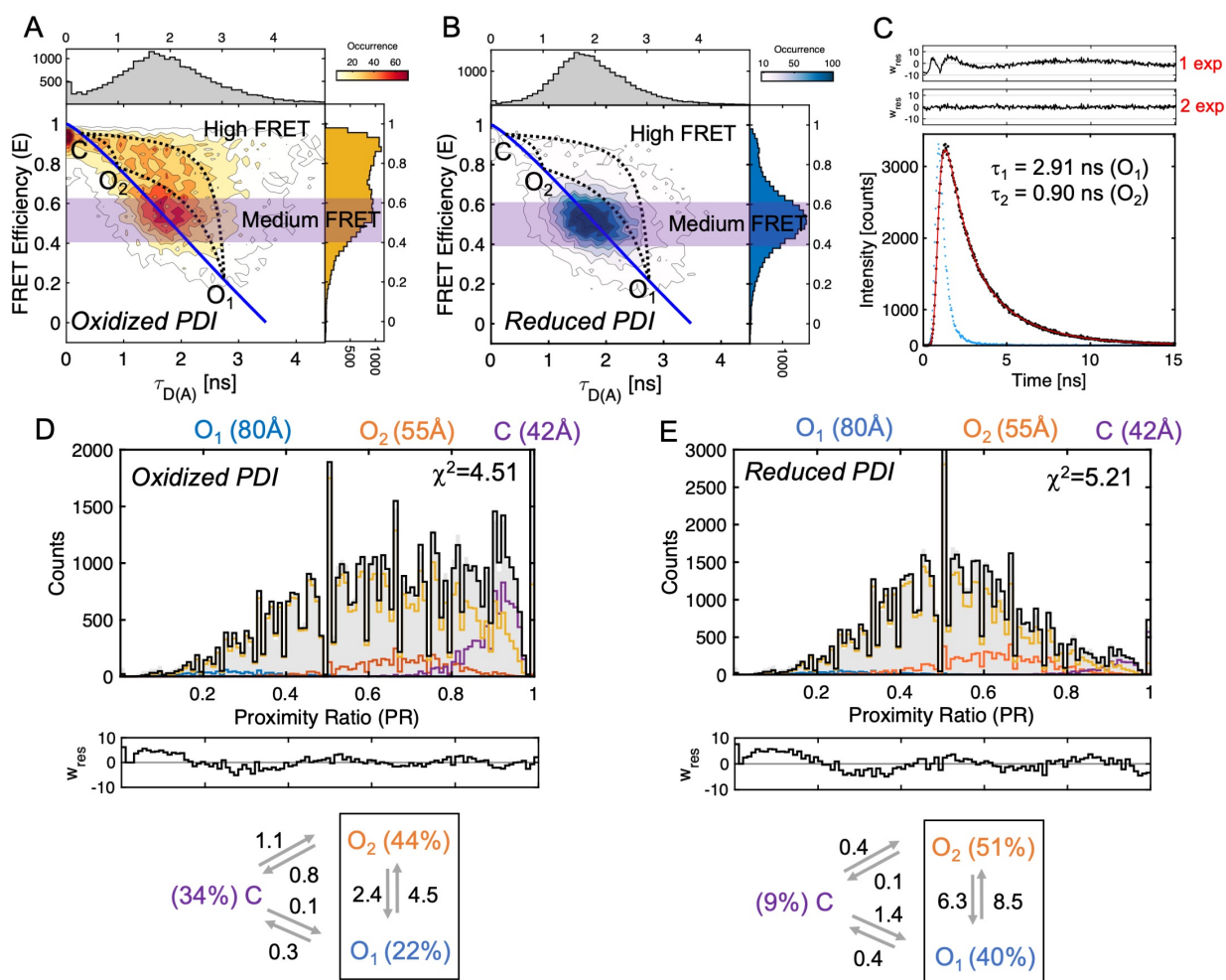3    the fit ($\chi^2$=1.28). This result agrees with our hypothesis and documents the existence of



**Figure 3. Dynamics of oxidized and reduced PDI.** 2D plots of FRET efficiency versus lifetime of the donor in the presence of the acceptor $\tau_{D(A)}$ for **(A)** oxidized and **(B)** reduced PDI 88/467 documenting the dynamic exchange between closed (high FRET) and open (medium FRET) ensembles. The solid blue line describes the theoretic relationship between FRET and lifetime ("static FRET line"). Systematic deviations from this relationship highlighted by the dotted lines track the trajectory of single molecules that are exchanging between C, $O_1$ and $O_2$ while passing through the confocal volume. The magenta regions indicate the molecules selected for the lifetime analysis (0.4-0.6) shown in **panel C**. **C)** Subpopulation specific fluorescence lifetime of oxidized PDI 88/467. Data points are in black. The red line represents the best fit obtained with a double exponential function ($\chi^2$=1.33). The value of lifetime of each population is shown in the plot. It is also reported in **Table 3** together with the amplitude for each population. The instrumental response function is shown in blue. Weighted residuals for one (1 exp) and two exponential (2 exp) fit are shown above the graph. PDA analyses of oxidized **(D)** and reduced **(E)** PDI 88/467 obtained with a dynamic three-state model. C, $O_1$ and $O_2$ sates are shown in purple, orange and blue, respectively while the exchange between them is represented by the yellow line. The black line represents the global fit. Weighted residuals are shown below each plot together with a diagram that summarizes the kinetic scheme, the rate constants and fraction of each population at equilibrium. Note how the residuals show a larger deviation toward lower values of PR. Such deviation is most likely due to acceptor fluorophore that goes into a dark, non-FRET state.

1   two states within the open ensemble, which we called $O_1$ and $O_2$. Additionally, we found
2   that the ratio $f_2/f_1$ between the amplitudes $f_2$ for $\tau_2$ and $f_1$ for $\tau_1$ was ~1.2 in both oxidized
3   and reduced PDI. We concluded that $O_2$ is more represented at equilibrium, regardless
4   of the redox state.

5       Previous studies have suggested that oxidized and reduced PDI are structurally
6   distinct (*16, 20, 32*). Despite the macroscopic differences between the FRET profiles, we,
7   however, measured values of $\tau_1$ and $\tau_2$ that are very similar, within experimental error
8   **(Table 3).** This indicates that very similar, perhaps identical, conformational states exist
9   in both oxidized and reduced PDI. Given PDI's flexibility, we propose that the redox
10  microenvironment modulates PDI by a conformational selection mechanism rather than
11  forming new macroscopic species.

12

13  **Connectivity between the ensembles and rate of interconversion**. By having
14  identified the minimum number of macroscopic states at equilibrium, we next defined the
15  connectivity between them (*23, 29*). To this end, using the previously determined values
16  of lifetime of 0.25 ns for C, 0.91 ns for $O_2$ and 2.75 ns for $O_1$, which, using the equation
17  $E=1-(\tau_{D(A)}/\tau_D)$, a $\tau_D$=3.5 ns and an $R_0$=65Å, correspond to $E_1$=0.93 (or 42Å) for C, $E_2$=0.73
18  (or 55Å) for $O_2$ and $E_3$=0.22 (or 80Å) for $O_1$, we drew the corresponding dynamic FRET
19  lines (dotted lines) in **Figure 3A** and **Figure 3B**. These lines were drawn according to
20  previous work in the field (*23-25, 30, 33*). Although less evident for reduced PDI because
21  of the low intensity of C, we found bursts lying on all three lines indicating dynamic
22  exchange between the FRET states. This led us to propose a triangular kinetic scheme
23  for both reduced and oxidized PDI, implying that, in solution, the three ensembles
24  spontaneously exchange to one another.

25      To quantify the abundance of each ensemble at equilibrium and determine the rates
26  at which they interconvert, we performed photon distribution analysis (PDA) (*25, 33, 34*).
27  Given the results of our previous experiments, we chose a three-state dynamic model.
28  Datasets for oxidized and reduced PDI 88/467 binned at 1, 0.75, 0.5 and 0.25 ms were
29  globally fit after fixing the value for each state to 42Å, 55Å and 80Å, which are the
30  experimentally determined values for C, $O_2$ and $O_1$ **(Figure S6)** and restricting the value
31  of sigma ($\sigma$) to 0.045. Sigma defines the width of a shot-noise limited distribution and was
32  experimentally determined in our system using fluorescently labeled double stranded
33  DNA constructs with different lengths **(Figure S7).** The value of 0.045 also agrees with
34  the results of recent studies aimed at comparing the accuracy and reproducibility of
35  smFRET data among multiple laboratories (*35*). Representative results obtained with
36  datasets binned at 0.5 ms are shown in **Figure 3D** and **Figure 3E** for oxidized and
37  reduced PDI 88/467, respectively. The rate constants measured by PDA are reported in
38  **Table 4** and summarized in the scheme located below each plot.

39      The most notable difference between the two redox sates identified by PDA concerns
40  the distribution of the three ensembles at equilibrium. In the presence of DTT **(Figure**

1    **3E)**, C was minimally populated (~9%) whereas $O_1$ and $O_2$ accounted for ~40% and

2    ~51%, respectively. By contrast, oxidized PDI spent similar amount of time in C and $O_1$

3    but preferred $O_2$. The fact that $O_2$ dominates agrees with our previous analysis and

4    suggests that $O_2$ is the preferred state adopted by unbound PDI in solution, regardless of

5    the redox state.

6      Other differences between the two redox sates concerned the magnitude of the rate

7    constants. We found that the rate at which $O_2$ converts to C ($k_{2,3}$) was ~8 time faster for

8    oxidized PDI compared to reduced PDI. In contrast, the rate at which C converts to $O_1$

9    ($k_{3,1}$) was ~9 times slower in oxidized PDI compared to reduced PDI. Faster $O_2 \rightarrow C$

10    conversion and slower $C \rightarrow O_1$ conversion explain why more C is present in oxidized PDI

11    compared to reduced PDI. We also found that the transition $O_1 \leftrightarrow O_2$ was the fastest of

12    the catalytic cycle, and significantly faster (~6 fold) than diffusion, especially for reduced

13    PDI. This latter observation is important for two reasons. First, it explains why $O_1$ and $O_2$

14    cannot be individually visualized in the 2D plots of FRET efficiency versus lifetime but

15    instead merge to form a broad ensemble. Second, it predicts that, when PDI dwells in

16    either $O_1$ or $O_2$, transition to C is energetically more expensive, especially when PDI is

17    reduced. From a structural standpoint, this indicates that $O_1$ and $O_2$ may be alike, yet

18    significantly different from C.

19      To further confirm that $O_1$ and $O_2$ exchange rapidly, we performed species selected

20    filtered fluorescence correlation spectroscopy (fFCS). In this method, as described by

21    Felekyan et al. (*36*), auto-correlation and cross-correlation functions are calculated for

22    two species of interest to determine the presence of dynamic exchange between them

23    and the interconversion rates. fFCS analysis was performed between $O_1$ (0.17<E<0.25)

24    and $O_2$ (0.65<E<0.75) in oxidized and reduced states. The results are shown in **Figure**
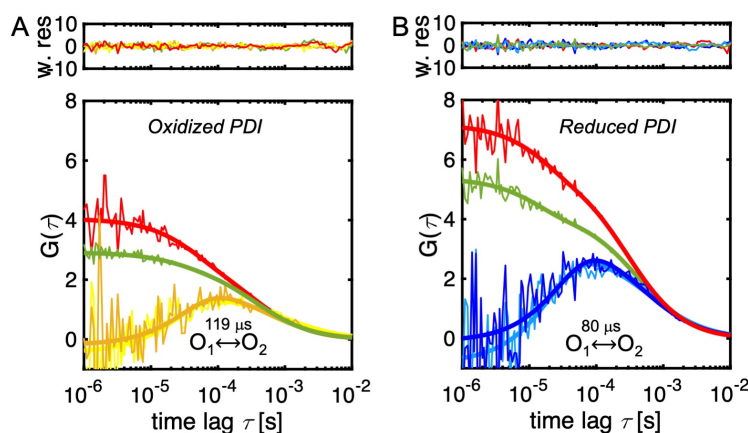
25    **4A** and **Figure 4B**.



**Figure 4. Rapid exchange between $O_1$ and $O_2$ ensembles monitored by fFCS.** Auto-correlation (red and green) and cross-correlation curves (yellow and blue) of $O_1$ and $O_2$ ensembles for oxidized **(A)** and reduced **(B)** PDI 88/467. The solid lines represent the best fit model obtained by globally fitting the four curves, which enables extraction of the interconversion time, expressed in microseconds. Randomly distributed weighted residuals are shown above each plot. Best fit parameters are $\tau_{R,ox}$ = 119±12 μs; $\tau_D$ = 469 μs (fixed, diffusion), $\chi^2$=1.11; $\tau_{R,rd}$ = 80±9 μs; $\tau_D$ = 469 μs (fixed, diffusion), $\chi^2$=1.25.

1    The presence of a bell-shaped cross-correlation function between $O_1$ and $O_2$
2    documents rapid exchange occurring on a time scale comparable or faster than the
3    diffusion time. Global fitting of the four correlation curves (two sACFs and two sCCFs)
4    required, in addition to the diffusion term ($\tau_D$), an additional relaxation term, $\tau_R$, providing
5    conclusive evidence of fast dynamics. After fixing the diffusion term to 469 $\mu s$ (see
6    methods), the values of $\tau_R$ calculated for oxidized and reduced PDI 88/467 were 119±12
7    $\mu s$ and 80±9 $\mu s$, respectively. These values are in reasonable agreement with the rate
8    constants measured by PDA for the $O_1 \leftrightarrow O_2$ exchange ($\tau_R = (k_{1,2} + k_{2,1})^{-1}$), which are 145
9    $\mu s$ for oxidized PDI and 67 $\mu s$ for reduced PDI, respectively. Thus, fFCS successfully
10   visualized rapid exchange between $O_1$ and $O_2$ and confirmed that one of the main
11   differences between oxidized and reduced PDI is the ability of $O_1$ and $O_2$ to exchange
12   faster in reduced PDI but slower in oxidized PDI.
13
14   **Nonequivalent structural role of the active sites**. PDI has two active sites, one in the
15   N-terminal **a** domain (C53/C56) and another one in the C-terminal **a'** domain
16   (C397/C400). To address how the four catalytic cysteines control the newly discovered
17   conformational equilibrium, they were mutated to the redox-insensitive amino acid alanine
18   (A) to generate the three new constructs, namely the quadruple mutant PDI
19   88/467/C53A/C56A/C397A/C400A (PDI-AA/AA), and the double mutants PDI
20   88/467/C53A/C56A (PDI-AA/CC) and PDI 88/467/C397A/C400A (PDI-CC/AA). After
21   verifying that the mutants had activity profiles consistent with what was previously
22   reported in the literature for the wild-type background (*37*) **(Figure S8)**, smFRET
23   measurements were collected in the absence and presence of DTT. PDA analysis was
24   used to quantify the species at equilibrium as described previously. Results of PDA
25   analysis are reported in **Table 4.** To facilitate comparison between PDI 88/467 wild-type
26   and mutants, 1D FRET efficiency plots are shown the main text **(Figure 5)**. 2D FRET
27   efficiency vs. lifetime plots are shown in the supplementary materials **(Figure S9)**.
28   A first important finding was that, in the absence of DTT, the active site variants were
29   similar to each other and also similar, yet not identical, to oxidized PDI 88/467 **(Figure 5,**
30   **top row)**. This data indicates that the catalytic cysteines are not required for initiating
31   large-scale domain movements such as those monitored here by smFRET. These
32   domain motions must, therefore, occur spontaneously, favored by the flexibility of the
33   protein fold. It is important to point out, however, that, even though the equilibrium
34   distribution of C, $O_1$ and $O_2$ remained mostly unchanged, the rates at which the three
35   states exchanged slightly decrease compared to PDI 88/467 **(Table 4)**, indicating that the
36   catalytic cysteines are important for protein dynamics.
37   Another important observation was that the active site mutants, while similar in the
38   oxidized state, behaved differently in the presence of DTT **(Figure 5, bottom row)**.
39   Specifically, PDI-AA/AA was insensitive to the addition of DTT; PDI-CC/AA behaved just
40   like PDI 88/467; and PDI-AA/CC was in between PDI-AA/AA and PDI-CC/AA insofar as

1   it partly responded to the addition of DTT, which led to a significant twofold accumulation
2   of C **(Figure 5C, bottom row)**. Importantly, this effect was not due to a reduced reactivity
3   of the mutant toward DTT, rather to changes in protein dynamics caused by the mutations.
4   This is because C never disappeared, even at very high (10 mM) concentrations of DTT
5   **(Figures 5D and 5E)**. We concluded that: 1) the active site cysteines are responsible for
6   sensing the redox microenvironment and 2) the N- and C-terminal active sites are
7   nonequivalent in the context of PDI dynamics.
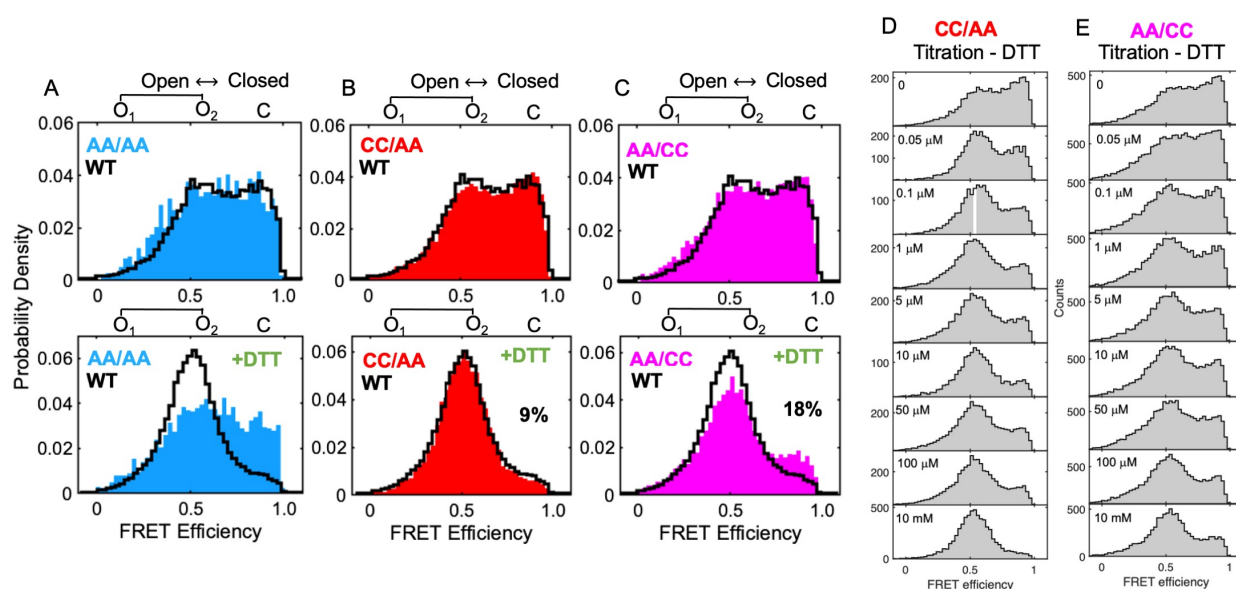


**Figure 5. Structural nonequivalence of the active sites.** Normalized 1D FRET efficiency histograms of **(A)** PDI 88/467 C53A/C56A/C397A/C400A (AA/AA, blue), **(B)** PDI 88/467 C397A/C400A (CC/AA, red) and **(C)** PDI C53A/C56A (AA/CC, magenta) overlaid to PDI WT (black) before (top panel) and after (bottom panel) the addition of 1 mM DTT. Note how PDI AA/AA is similar to oxidized PDI 88/467 wild-type (WT) and insensitive to DTT and how the mutations C53A and C56A led to a macroscopic accumulation of C, which, according to PDA analysis **(Table 4)** increased 2-times, from 9% to 18%. 1D FRET efficiency histograms of PDI 88/467 C397A/C400A (CC/AA) **(D)** and PDI C53A/C56A (AA/CC) **(E)** collected at increasing concentrations of DTT (0-10 mM), covering 4 orders of magnitudes.

8

9   **Active site ligation stabilizes closed conformations of PDI.** To further investigate the
10  role of the active sites in controlling the allosteric equilibrium, we took advantage of their
11  reactivity toward the commercially available inhibitor 16F16 (*38*), which contains a
12  chloroacetamide electrophile for covalent modification of PDI. In contrast to commonly
13  used alkylating agents such as N-ethylmaleimide (NEM) and diamide, 16F16 is more
14  potent and specifically react with the active site cysteines C53 and C397 (*39*).
15  Furthermore, at the concentration used in this study, 16F16 does not quench the
16  fluorescence intensity of the Atto dyes, which was significantly compromised with mM
17  concentrations of NEM and diamide. The results of this experiment are shown in **Figure
18  6A** and **Figure 6B.** Starting from a solution of oxidized PDI 88/467, we added, in a
19  sequential order, 50 μM DTT and then, after 70 min, 50 μM 16F16. Addition of DTT and
20  16F16 are indicated with red arrows. This design enabled us to follow in real-time PDI

1  conformational cycle. We found that addition of 16F16 to reduced PDI shifted the

2  equilibrium toward the closed ensemble in a time-dependent fashion. Since 16F16 did

3  not change the FRET profile of oxidized PDI *(data not shown)*, we interpreted this as

4  evidence that binding of 16F16 followed by alkylation of the catalytic cysteines stabilizes

5  closed conformations of PDI. Similar results were obtained with another commonly used

6  irreversible active site inhibitor of PDI, namely PACMA-31 **(Figure 6C)** (*40*), arguing for a

7  general mechanism of this class of compounds.

8     To independently validate this observation, we performed SEC experiments using PDI

9  wild-type free and bound to 16F16 and PACMA-31 **(Figure 6D)**. The retention volume of

10  PDI was delayed of ~0.4 ml in the presence of 16F16 and PACMA-31 compared to

11  unbound PDI. Since proteins with smaller hydrodynamic radius have larger retention

12  volumes, this result supports the compaction model upon ligation inferred by smFRET
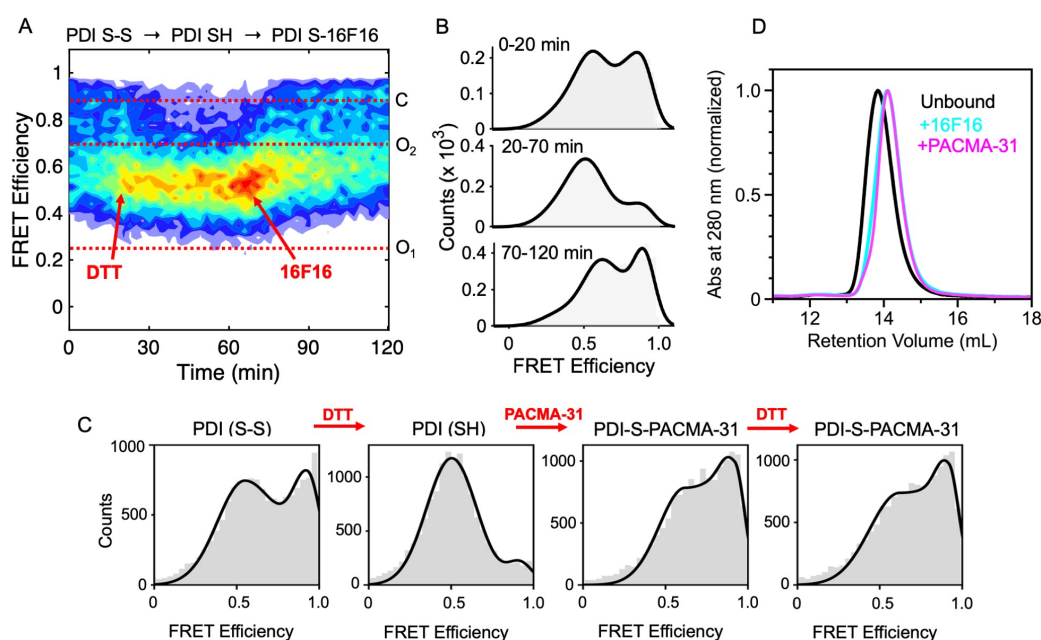
13  data.



**Figure 6**. **Active site ligation stabilizes closed conformations of PDI.** A solution of PDI 88/467 (50 pM) was continuously monitored for 120 min under different experimental conditions. Addition of 50 $\mu$M DTT and 50 $\mu$M 16F16 is indicated with red arrows. The horizontal dotted lines identify the mean FRET efficiency value of C, $O_1$ and $O_2$. **B)** FRET efficiency histograms of PDI 88/467 at three different time intervals monitoring key steps of the reaction of PDI 88/467 with 16F16. **C)** FRET histograms of PDI 88/467 (100 pM, TBSE-T) in the absence and presence of DTT (1 mM) before and after the addition of 50 $\mu$M PACMA-31. Note how PACMA-31, like 16F16, shifts the conformational equilibrium towards the closed ensemble. Further addition of DTT is inconsequential. This is because PACMA-31 reacts irreversibly with the active site thiol groups of PDI to form a covalent adduct. **D)** SEC analysis of PDI free and bound to 16F16 (cyan) and PACMA-31 (magenta).

14

15  **Discussion**

16  This study reports a detailed biophysical characterization of PDI's dynamics in solution

17  and identifies several new features of this allosteric enzyme that were not known before.

1   Using a combination of four novel FRET pairs located in the **a** and **a'** catalytic domains
2   and three active site mutants, we discovered that PDI visits, on the sub-millisecond
3   timescale, three major conformational ensembles at equilibrium, $O_1$, $O_2$ and C, whose
4   distribution is regulated by a variety of factors, namely the redox microenvironment
5   **(Figure 2)**, the presence of active site cysteines **(Figure 5)** and active site ligands **(Figure**
6   **6)**. Importantly, the identification of these ensembles is fully consistent with previous
7   structural, biophysical, and biochemical data documenting structural flexibility of the
8   protein fold (*16, 18-20, 32*). It thus represents an important step forward for achieving a
9   deeper mechanistic understanding of how this enzyme works under physiologically
10  relevant conditions.
11  While PDI's flexibility was expected, the discovery that the microenvironment
12  modulates PDI by a conformational selection mechanism is conceptually new. As such,
13  this finding enables us to propose a new model of PDI dynamics whereby environmental
14  factors commonly found in cells and in the circulation, such as high levels of levels of
15  oxidative stress and chemical modifications of catalytic cysteines (i.e., sulfenylation, S-
16  nitrosylation and acylation) affect the solution structure of PDI by shifting this equilibrium
17  without forming new macroscopic species. Selection between pre-existing PDI
18  ensembles provides the structural basis for understanding how PDI activity is regulated
19  by conformational modulation.
20  Also new and illuminating is the finding that, despite undergoing large conformational
21  changes, $O_1$, $O_2$ and C, interconvert very rapidly. Energetically, this indicates that the
22  free-energy landscape of PDI is characterized by low basins and shallow minima. To
23  visualize this, we calculated free-energy barriers for transition between the ensembles
24  using the Arrhenius equation and the reaction rate constants reported in **Table 4 (Figure**
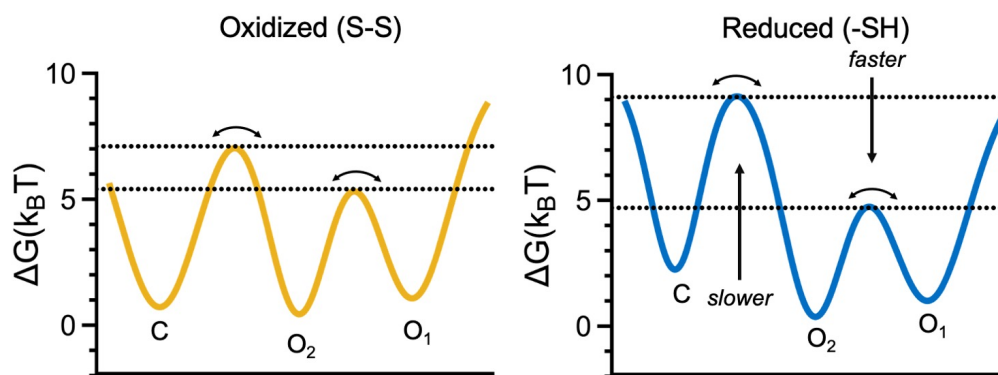


**Figure 7**. **Conformational landscape of PDI inferred by smFRET.** Free energy profiles of oxidized (left, yellow) and reduced (right, blue) PDI obtained using data reported in **Table 4**. Barrier heights corresponding to $C \rightarrow O_2$ and $O_1 \rightarrow O_2$ (horizontal lines) for oxidized and reduced PDI were calculated using the Arrhenius equation with a pre-exponential factor of $10^5 \, s^{-1}$. $k_B$ is the Boltzmann constant and T is the temperature. The distributions were arbitrarily drawn using a combination of Gaussian distributions. Note how in the presence of DTT the free-energy barrier increases for the $C \leftrightarrow O_1/O_2$ transition (slower transition) whereas it decreases for the $O_1 \leftrightarrow O_2$ transition (faster transition) leading to redistribution of the conformational ensembles.

**7).** Quite remarkably, these calculations yielded Gibbs free-energy values ($\Delta$G) lower than 10$K_B$T, which is the energy required to form/break less than two hydrogen bonds (6.7$K_B$T is the energy calculate for one hydrogen bond using the same pre-exponential factor used by us and others (*41*)). Considering the magnitude of the conformational changes monitored by smFRET and the low free-energy barriers required for transitioning between the states, we propose that, in solution, PDI's flexibility arises from rapid relocations of the domains mediated by the linkers. To satisfy these energetic requirements, the linkers, however, must be free to move, thus only weakly interacting with the surrounding domains. While more studies are needed to validate this model, recent results obtained in our laboratory with the FRET pair 308/467 (*22*), in which dyes are located across linker 3, also known as the x-linker, supports this view. In fact, PDI 308/467 not only displays multiple FRET states at equilibrium but also displays kinetic features that are similar, yet not identical, to the one reported here for FRET pairs located in the **a** and **a'** domains. Considering these new findings, alternative models predicting the x-linker to mediate PDI dynamics by binding and dissociating with a hydrophobic pocket in **b'** (*42-44*) should be reconsidered.

Another interesting observation emerging form our smFRET analysis of PDI was that the FRET profile of the redox-insensitive variant PDI AA/AA was similar to the FRET profile of oxidized PDI, not reduced PDI. This result was unexpected based on previous literature (*16, 20*) and indicates that, while active site thiols are necessary to drive conformational changes in PDI, the presence of disulfide bonds is not. While the structural basis behind this observation cannot be inferred by these studies, because of the different pKa values between the two cystine residues of the catalytic motif (*1*), we speculate that protonation of the resolving cysteine may be key to initiate this process.

Finally, PDI interacts with many substrates intracellularly and extracellularly. The mechanisms of substrate recognition and release are not fully understood. To date, the most popular model for PDI-assisted catalysis is based on X-ray crystal data (*16*) and envisions oxidized PDI adopting a flexible open form, which is primed for substrate binding. After transferring the disulfide bond to the substrate, reduced PDI is then believed to become more compact and rigid, thus favoring substrate release (*16, 20, 32*). Evaluation of PDI by smFRET led to identification of new structural features that challenge this model. In contrast with what was predicted by X-ray crystallography**,** our data indicate that residues 57/467 and residues 88/467 spend significantly more time away from each other in reduced PDI compared to oxidized PDI. In solution, the catalytic domains of reduced PDI may therefore visit conformations that are significantly more open than what has been captured by X-ray crystallography. At the same time, residues 57/467 and residues 88/467 spend significantly more time close to each other in oxidized PDI compared to reduced PDI. On these bases, we propose an alternative conformational cycle for PDI whereby oxidized PDI can adopt very compact conformations upon substrate binding and, therefore, substrate release is facilitated by opening, not closing,

1  of the structure. This mechanism agrees well with findings in **Figure 6** documenting that
2  active site ligation favors closed conformations of PDI. It could also explain how reduced
3  PDI, which is, on average, more open than oxidized PDI, can easily interact and process
4  with very bulky substrates such as clotting factors.
5
6  **Materials and Methods**
7  **Protein production and purification.** The cDNA of human PDI (residues 18-479) was
8  cloned into a pBAD vector expression system (ThermoFisher) and modified to include an
9  N-terminal 6 his-tag and a C-terminal Avitag. Genetic incorporation of the unnatural amino
10 acidic N-Propargyl-L-Lysine (Prk) (SiChem) at positions 57, 88, 401 and 467 was
11 obtained using the AMBER suppressor pyrrolysine tRNA/RS system from
12 *Methanosarcina mazei*. Mutations C53A, C56A, C397A, C400A in the 88/467 background
13 were generated using the Quickchange Lightning kit (Agilent) with appropriate primers.
14 Sequence verified PDI variants (Genewiz) were expressed in Top10 cells and purified
15 following recently published procedures (*22*).
16
17 **Protein labeling.** Site-specific labeling was achieved as detailed elsewhere (*22*). Briefly,
18 a solution of 25 µM of PDI in 1x phosphate buffer saline (PBS) pH 7.4 (Corning) was
19 reacted with 4x molar excess of azide dyes (donor, acceptor or donor/acceptor mixtures)
20 (Sigma-Aldrich) in the presence of 150 µM copper sulfate ($CuSO_4$), 750 µM tris-
21 hydroxypropyltriazolylmethylamine (THPTA), and 5 mM sodium ascorbate. The reaction
22 mixer was left on slow rotisserie for 1 hour 30 minutes at room temperature, then 30
23 minutes on ice. The reactions were stopped by adding 5mM EDTA. Monomeric PDI was
24 successfully separated by protein aggregates by size exclusion chromatography (SEC),
25 using a Superdex 200 10/300 column (Cytiva) equilibrated with Tris 20 mM (pH 7.4), 150
26 mM NaCl, 2 mM EDTA. The quality of each protein preparation was assessed by
27 NuPAGE Novex 4–12% Bis-Tris protein gels (ThermoFisher). Gels were stained with
28 Coomassie Brilliant Blue R-250 (ThermoFisher) and scanned on a Typhoon imager
29 (Cytiva) at 532 nm and 633 nm to verify specific incorporation of the fluorescent dyes.
30 Total protein concentration was determined by reading the absorbance at 280, using a
31 molar coefficient adjusted for the amino acidic sequence of each variant. The
32 concentration of Atto-550 and Atto-647N was calculated by reading the absorbance at
33 550 nm and 640 nm, respectively. Typical labeling efficiencies were 90%.
34
35 **Circular Dichroism (CD).** Far-UV CD spectra were recorded on Jasco J-715
36 spectropolarimeter equipped with a water-jacketed cell holder, connected to a water-
37 circulating bath, as done before (*22*). Spectra were collected for unlabeled and labeled
38 protein in PBS with 2mM EDTA at a concentration of 0.12 mg/ml. The final spectra
39 resulted from the average of five accumulations after base line subtraction.
40

1    **Intrinsic Fluorescence Assay.** Intrinsic fluorescence spectra (tryptophan) were
2    performed in a reaction volume of 200 µl with 0.2 µM of PDI in 20 mM Tris-HCl buffer
3    containing 150 mM NaCl (pH 7.4) and either 1mM GSH or 1mM GSSG were incubated
4    for 1hr at room temperature. Emission spectra were recorded at 295–450 nm with
5    excitation at 280 nm using a FluoroMax-4 (Horiba).
6
7    **Insulin reductase assay.** PDIs (400 nM) were solubilized in PBS and then added to a
8    solution containing 0.2 mM human insulin (Sigma-Aldrich), 2 mM EDTA and 325 µM DTT.
9    The reaction was monitored at 650 nm (turbidity due to precipitation of the product) for
10    1 h at 25 °C using a Spectramax i3 (Molecular Devices). Statistical analysis was
11    performed using unpaired t-test in Prims 9.0.
12
13    **Determination of Anisotropy and Quantum Yield.** Four singly labeled PDI constructs
14    (i.e., K57U, S88U, K401U and K467U) were expressed, labeled with either Atto-550 or
15    Atto-647N and purified as described before for anisotropy and quantum yield
16    determination. Anisotropy was recorded in 1x PBS with 2 mM EDTA buffer using
17    Fluorolog-3 (Jobin-Yvon). The Atto-550 labeled proteins (50 nM) were excited at 540 nm
18    and emission was monitored at 580 nm. The Atto-647N labeled proteins (50nM) were
19    excited at 640 nm and emission was monitored at 680 nm, excitation and emission slits
20    were set at 1 and 14 nm, respectively. The donor quantum yield was measured in bulk
21    fluorescence assays in a FluoroMax-4 (Jobin–Yvon) for each donor position, in reference
22    to the quantum yield of Rhodamine 110 (89.87+/-0.91). The emission spectra of PDI
23    labeled with only a donor at positions 57, 88, 401 and 467 were collected at five
24    concentrations under the same excitation conditions (532 nm) in the buffer used for
25    smFRET experiments. The quantum yield was found from the ratio between the dye's
26    integrated emission spectrum and its absorbance at 532 nm. The overlap between the
27    donor emission spectrum and the acceptor absorbance spectrum is defined as:

28   
$$J(\lambda) = \int_0^\infty F_D(\lambda)\, \varepsilon_A(\lambda)\lambda^4 \mathrm{d}\lambda$$

29    Where $F_D(\lambda)$ is the normalized donor emission spectrum, and $\varepsilon_A$ is the acceptor's
30    absorbance spectrum, measured for PDI labeled with an acceptor at position at position
31    57, 88, 401 and 467 respectively.
32
33    **Single-molecule FRET measurements.** FRET measurements of freely diffusing single
34    molecules were performed with a confocal microscope MicroTime 200 (PicoQuant) using
35    published procedures (*22, 45, 46*). Excitation laser light from 532 nm and 638 nm lasers
36    was used to excite the donor and acceptor fluorophores, respectively. A Pulsed
37    Interleaved Excitation (PIE) setup was used with a pulse rate of 20 MHz to alternate the
38    donor and acceptor excitation. PIE reports the status of both donor and acceptor
39    fluorophores by sorting molecules based on relative donor:acceptor stoichiometry (S) and

1    apparent FRET efficiency (E), as described before (*24, 30, 47, 48*). A dichroic mirror
2    (ZT405/488/532/640rpc-XT, Chroma) reflecting at 532 and 638 nm guided the light to a
3    high numerical aperture apochromatic objective (60x, N.A. 1.2, water immersion,
4    Olympus) that focused the light to a confocal volume of 1.0 fl. Fluorescence from excited
5    molecules was collected with the same objective and focused onto a 50-µm diameter
6    pinhole. The donor and acceptor emissions were separated via a dichroic filter with a
7    dividing edge at 620 nm (620DCXR, Chroma). Suited bandpass filters (HQ580/70m,
8    Chroma and HQ690/70m, Chroma) were inserted to eliminate the respective excitation
9    wavelength and minimize spectral crosstalk. The fluorescence was detected with two
10   single-photon avalanche diode detectors (τ-SPAD, Perkin Elmer) using Time-correlated
11   Single Photon Counting with the TimeHarp 200 board (HydraHarp 400, PicoQuant). Data
12   were stored in the Time-tagged Time-resolved Mode as a PTU file format.

13       Measurements were performed 25 µm deep in the solution using a laser power of ~15
14   µW. Total acquisition time was ~40 minutes per sample. Data collection was repeated for
15   a minimum of four times using the same sample as well as new protein samples from at
16   least one different preparation. Identical results were obtained in all cases, indicating
17   stability of the protein sample during data collection and reproducibility. Concentration
18   was 50-100 pM of labeled protein solubilized in 200 µl of 20 mM Tris, 150 mM NaCl, 2
19   mM EDTA, 0.003% Tween 20, pH 7.4 (TBSE-T) for oxidized PDI and TBSE-T with 1 mM
20   DTT for reduced PDI. DTT titrations were performed by preincubating oxidized PDI with
21   the desired concentration of DTT for 40 minutes at room temperature before data
22   collection to ensure equilibrium. However, similar results were obtained by adding
23   increasing concentrations of DTT to the same protein sample, implying fast reactivity of
24   DTT towards the enzyme. The PDI inhibitors 16F16 (Sigma-Aldrich) and PACMA-31
25   (Sigma-Aldrich) solubilized in DMSO were added to the solution at a final concentration
26   of 50 µM. The inhibitory effect of 16F16 and PACMA-31 was verified in the insulin
27   reductase assay, as detailed above. Data recording was performed using the Sympho-
28   Time Software 64, version 2.3 (PicoQuant, Berlin).
29
30   **Single-molecule FRET analysis.** Data analysis was carried out with the Matlab-based
31   software PAM (*49*) using a customized profile optimized for our microscope. Signals from
32   single molecules were observed as bursts of fluorescence. Bursts with more than 40
33   counts were searched with the All Photon Burst Search (APBS) algorithm. Integration
34   time was set to 0.5 ms. Appropriate corrections for direct excitation of the acceptor at the
35   donor excitation wavelength (DE), leakage of the donor in the acceptor channel (Lk), and
36   the instrumental factor ($\gamma$) were determined experimentally using a mixture of double-
37   stranded DNA models with known FRET efficiency and stoichiometry labeled with dyes
38   Atto-550 and Atto-647N. These are: DE=0.05, Lk=0.08, $\gamma$=0.85.
39       A plot of the stoichiometry versus the ALEX-2CDE filter was used to determine the
40   required upper threshold that removes donor-only (S=1) and acceptor-only (S=0)

1     molecules. In general, only molecules within the range S = 0.25–0.75 were considered in
2     the final analysis. Doubly labeled photobleached molecules were further eliminated using
3     the ALEX-2CDE (<14) and |TDX-TAA| (<0.5) filters as described before by Tomov et
4     al.(*50*) and Kudryavtsev et al.(*24*), respectively. These stringent filters guarantee
5     elimination of unwanted signal, as described before (*24*).

6     Lifetime was calculated using PAM after correction for instrument response factor
7     (IRF). For the whole dataset, a double exponential decay function was used for the donor
8     channel whereas a single exponential decay function was used for the acceptor channel
9     (*49*). Static and dynamic FRET lines were generated using PAM following previously
10    published methods (*24, 25, 30*) and using an apparent linker length of 5 Å.

11    Subpopulation specific fluorescence lifetime analysis was also performed using PAM.
12    However, for this type of analysis, the region of interest was first selected in the
13    BurstBrowser module. Data were then systematically fit with one, two and three
14    exponential functions to identify the best fit. Decisions were made based on analysis of
15    the weighted residuals. Donor only and acceptor only species were also selected to verify
16    that, in contrast to the FRET interval belonging to the open ensemble, they satisfactory fit
17    a single exponential decay.

18    Theoretical FRET values were obtained by coarse-grained simulations using the
19    FRET-restrained positioning and screening (FPS) software (*51*). The dye dimensions
20    were estimated to be 7.8, 4.5, and 1.5 Å for Atto-550 and 7.15, 4.5 and 1.5 Å for Atto-
21    647N after minimization of their chemical structure using Maestro (Schrödinger). The
22    linker lengths and widths used were 18 and 4.5 Å for both dyes. After performing
23    accessible volume (AV) simulations, the corresponding mean transfer efficiency was
24    calculated by assuming rapid fluctuations of the interdye distance occurring on time
25    scales similar to the fluorescence lifetime of the donor (∼3.4 ns in the absence of the
26    acceptor). This assumption is justified based on the anisotropy values reported in **Table**
27    **1** obtained for the labeled proteins.

28

29    **Dynamic Photon Distribution Analysis (PDA).** PDA analysis was performed using the
30    PDAfit module built in PAM. Proximity histograms were reconstructed by binning the
31    same dataset at 0.25, 0.5, 0.75, and 1 ms. Histogram library with a grid resolution for
32    E=100 and a minimum number of photons of 10 per bin were chosen. The datasets were
33    then fit using a dynamic three-state model. Distances calculated from lifetime analysis
34    were fixed. The width of the distance distribution was also fixed at sigma=0.045. This was
35    determined from the measurement of several static double-stranded doubly labeled DNA
36    **(Figure S6)**. To assess robustness of the fit, PDA was repeated by systematically varying
37    the initial value of the rate constants to 1, 0.5 and 0.75 ms$^{-1}$ (min 0, max 10) while keeping
38    the other settings identical. The results in **Table 4** represent the average of these three
39    independent determinations.

40

**Species Selected Filtered FCS (fFCS).** Data were collected using the same setup described before in which we added two SPAD detectors (Excelitas Technologies) for a total of two parallel and two perpendicular detectors and increased the laser power to ~30 $\mu$W. Briefly, the light was simultaneously split (50:50) and rotate by a polarizing cube. While the configuration of the perpendicular path is described before, the configuration of the parallel path is the following: dichroic filter ZT633rdc-UF1 (Chroma), donor emission filter ET585/65m (Chroma), and acceptor emission filter ET700/75 (Chroma). Fine-tuning of the system was performed such as very similar fluorescent intensity values (5% difference) were obtained for the two sets of detectors. FRET efficiency histograms and values of lifetime obtained for the 2- and 4-SPADs setups were identical.

Species selected filtered-Fluorescence Correlation Spectroscopy analysis was done using BurstBrowser module from PAM software. Microtime patterns for $O_1$ and $O_2$ states were obtained using FRET efficiency thresholds around the mean lifetime values obtained for $O_1$ (E=0.17 to 0.25) and $O_2$ (E=0.65 to 0.75) states. Signals from selected FRET efficiency region were cross-correlated after generating the appropriate TCSPC filters for the parallel and perpendicular channels. This eliminates the dead-time of TCSPC hardware and SPAD detectors. Four correlations functions, two auto correlation functions and two cross correlations functions between the species $O_1$ and $O_2$ were generated. The four curves were globally fitted using a single-component diffusion and single exponential kinetic term, as described by Felekyan et al. (*36*) and letting the amplitude for cross-correlation assume negative values. fFCS fit was carried out in FCSfit module from PAM. The diffusion time was fixed to 469 $\mu$s. This value was obtained from independent FCS measurements of reduced and oxidized PDI molecules at nanomolar concentrations. The ratio of the axial and lateral size of the confocal volumes were globally fixed, $\rho$=4.6. This was obtained from independent FCS measurements using singly labeled calibration samples such as double strand DNA or singly labeled PDI molecules at nanomolar concentrations. Capabilities of fFCS was tested using Holliday Junctions, as described elsewhere (*36*).

**Size exclusion chromatography analyses.** 100 $\mu$L (100 $\mu$g) of a solution of PDI unbound and treated with 100 $\mu$M 16F16 or 100 $\mu$M PACMA-31 after reduction with DTT for 90 minutes at room temperature were loaded into a Superdex 200 HR 10/300 (Cytiva, USA) at a flow rate of 0.5 ml/min that was equilibrated with in Tris 20 mM, 150 mM NaCl at pH 7.4, 5 mM EDTA. Absorbance was monitored at 280 nm using an ÄKTApurifier system (Cytiva, USA).

**Data availability.** All data are contained in the manuscript. PTU files are made available upon reasonable request by contacting the authors.

**Table 1. Anisotropy and quantum yield (Φ) values for singly labeled PDI mutants.**

|  | Atto-500 | | Atto-647N | |
|---|---|---|---|---|
|  | **Anisotropy** | **Quantum yield** | **Anisotropy** | **Quantum yield** |
| **K57U** | 0.23±0.03 | 0.77±0.05 | 0.24±0.03 | 0.63±0.05 |
| **K88U** | 0.19±0.02 | 0.79±0.05 | 0.18±0.01 | 0.65±0.03 |
| **K401U** | 0.22±0.01 | 0.78±0.02 | 0.22±0.01 | 0.64±0.02 |
| **K467U** | 0.21±0.02 | 0.79±0.03 | 0.21±0.02 | 0.65±0.02 |

Experimental conditions are 100 mM potassium phosphate (pH 7.4), 2 mM EDTA, at 25°C. For anisotropy determination, the concentration of PDI was 10 nM, ex 540/em 580 for Atto-550 and ex640/em680 for Atto-647N, ex/em slits 1 and 14 nm, respectively. The results represent the average of two independent determinations. For quantum yield determination Rhodamine 110(Φ=0.89±0.02) in ethanol was used as a standard, for free dyes in buffer, Atto-550(Φ=0.79±0.02) and Atto-647N (Φ=0.64±0.02) were also experimentally determined.

**Table 2. Summary of FRET (E) and Stoichiometry values (S) for the PDI variants measured in the absence (top) and presence (bottom) of DTT.**

| | Average E | STD E | Average S | STD S |
|---|---|---|---|---|
| **57/401** | 0.82 | 0.16 | 0.48 | 0.094 |
| **57/467** | 0.61 | 0.24 | 0.50 | 0.104 |
| **88/401** | 0.82 | 0.16 | 0.50 | 0.096 |
| **88-467** | | | | |
| **WT** | 0.66 | 0.22 | 0.52 | 0.098 |
| **AAAA** | 0.64 | 0.22 | 0.51 | 0.099 |
| **AACC** | 0.65 | 0.22 | 0.53 | 0.098 |
| **CCAA** | 0.67 | 0.21 | 0.51 | 0.099 |

| | Average E | STD E | Average S | STD S |
|---|---|---|---|---|
| **57/401** | 0.80 | 0.17 | 0.48 | 0.085 |
| **57/467** | 0.54 | 0.19 | 0.51 | 0.100 |
| **88/401** | 0.79 | 0.18 | 0.50 | 0.095 |
| **88-467** | | | | |
| **WT** | 0.53 | 0.17 | 0.52 | 0.090 |
| **AAAA** | 0.64 | 0.22 | 0.51 | 0.098 |
| **AACC** | 0.56 | 0.21 | 0.50 | 0.090 |
| **CCAA** | 0.54 | 0.16 | 0.51 | 0.085 |

Average FRET and Stoichiometry values and corresponding errors were determined using the BurstBrowser module in PAM.

**Table 3. Subpopulation specific (0.4-0.6) fluorescence lifetime analysis of oxidized and reduced PDI 88/467**

|  | $\tau 1$ (ns) | f1 | $\tau 2$ (ns) | f2 | $X^2$ |
|---|---|---|---|---|---|
| **oxidized 88-467** |  |  |  |  |  |
| **1 exp** | 2.23 ± 0.08 | 1 | - | - | 9.69 |
| **2 exp** | 2.91 ± 0.15 | 0.44 | 0.90 ± 0.06 | 0.56 | 1.32 |
| | | | | | |
| **reduced 88-467** |  |  |  |  |  |
| **1 exp** | 2.04 ± 0.08 | 1 | - | - | 14.58 |
| **2 exp** | 2.72 ± 0.15 | 0.42 | 0.91 ± 0.06 | 0.58 | 1.32 |

Values of lifetime are indicated by $\tau$. The fraction of each population (0-1) is indicated by **f**. The quality of the fit is expressed by the value of $X^2$. The same dataset was fit with one, two and three exponential functions using the lifetime fit module in PAM. Satisfactory fit was attained for both oxidized and reduced PDI with a two exponential decay model. Since no further improvement was observed with a three exponential models, this result was discarded and not presented in the Table.

**Table 4. PDA analysis of oxidized (top) and reduced (bottom) PDI**

| Rates (ms$^{-1}$) | WT | AA/AA | CC/AA | AA/CC |
|---|---|---|---|---|
| $k_{1,2}$ | 4.50 ± 0.81 | 2.14 ± 0.14 | 4.43 ± 0.05 | 2.73 ± 0.36 |
| $k_{1,3}$ | 0.32 ± 0.31 | 0.63 ± 0.23 | 0.34 ± 0.13 | 0.26 ± 0.28 |
| $k_{2,1}$ | 2.38 ± 0.36 | 1.59 ± 0.13 | 2.39 ± 0.09 | 1.51 ± 0.11 |
| $k_{2,3}$ | 0.78 ± 0.26 | 1.03 ± 0.09 | 0.67 ± 0.06 | 0.68 ± 0.12 |
| $k_{3,1}$ | 0.15 ± 0.11 | 0.66 ± 0.15 | 0.12 ± 0.02 | 0.48 ± 0.24 |
| $k_{3,2}$ | 1.07 ± 0.24 | 0.95 ± 0.11 | 0.94 ± 0.06 | 0.66 ± 0.24 |
| **% state** | | | | |
| $O_1$ (80 Å) | 22 ± 1 | 29 ± 1 | 22 ± 1 | 26 ± 1 |
| $O_2$ (55 Å) | 44 ± 3 | 36 ± 2 | 43 ± 1 | 42 ± 2 |
| C (42 Å) | 34 ± 1 | 35 ± 2 | 35 ± 1 | 32 ± 1 |
| $\chi 2$(global) | 5.5 | 6.2 | 5.2 | 4.9 |

| Rates (ms$^{-1}$) | WT | AA/AA | CC/AA | AA/CC |
|---|---|---|---|---|
| $k_{1,2}$ | 8.49 ± 1.95 | 2.12 ± 0.15 | 9.35 ± 0.30 | 4.33 ± 1.29 |
| $k_{1,3}$ | 0.36 ± 0.33 | 0.39 ± 0.34 | 0.99 ± 0.66 | 1.03 ± 1.04 |
| $k_{2,1}$ | 6.28 ± 1.07 | 1.45 ± 0.39 | 7.50 ± 1.95 | 3.52 ± 0.32 |
| $k_{2,3}$ | 0.11 ± 0.06 | 0.75 ± 0.59 | 0.75 ± 1.19 | 0.27 ± 0.09 |
| $k_{3,1}$ | 1.39 ± 0.84 | 0.48 ± 0.17 | 3.95 ± 4.47 | 0.79 ± 0.19 |
| $k_{3,2}$ | 0.40 ± 0.21 | 0.97 ± 0.23 | 2.05 ± 2.72 | 0.50 ± 0.50 |
| **% state** | | | | |
| $O_1$ (80 Å) | 40 ± 1 | 28 ± 1 | 42 ± 1 | 37 ± 3 |
| $O_2$ (55 Å) | 51 ± 3 | 37 ± 2 | 49 ± 3 | 45 ± 6 |
| C (42 Å) | 9 ± 2 | 35 ± 1 | 9 ± 2 | 18 ± 3 |
| $\chi 2$(global) | 4.5 | 5.1 | 4.2 | 5.2 |

PDA was performed on dataset binned at 0.25, 0.5, 0.75 and 1 ms. Photons from each burst were used to build a proximity ratio (PR) histogram. The resulting histogram was then fitted using a Monte Carlo approach for simulating the burst-wise histogram using a dynamic three-state model. To assess robustness of the fit, PDA was repeated by systematically varying the initial value of the rate constants to 1, 0.5 and 0.75 ms$^{-1}$ (min 0, max 10) while keeping the other settings identical. The results in the tables represent the average of these three independent determinations.

## References

1. F. Hatahet, L. W. Ruddock, Protein disulfide isomerase: a critical evaluation of its function in disulfide bond formation. *Antioxid Redox Signal* **11**, 2807-2850 (2009).

2. M. Matsusaki *et al.*, The Protein Disulfide Isomerase Family: from proteostasis to pathogenesis. *Biochim Biophys Acta Gen Subj*, (2019).

3. L. Ellgaard, L. W. Ruddock, The human protein disulphide isomerase family: substrate interactions and functional properties. *EMBO Rep* **6**, 28-32 (2005).

4. Y. Wu, D. W. Essex, Vascular thiol isomerases in thrombosis: The yin and yang. *J Thromb Haemost*, (2020).

5. L. Wang, J. Yu, C. C. Wang, Protein disulfide isomerase is regulated in multiple ways: Consequences for conformation, activities, and pathophysiological functions. *Bioessays*, e2000147 (2020).

6. P. V. S. Oliveira *et al.*, Protein disulfide isomerase plasma levels in healthy humans reveal proteomic signatures involved in contrasting endothelial phenotypes. *Redox Biol* **22**, 101142 (2019).

7. M. Matsusaki *et al.*, The Protein Disulfide Isomerase Family: from proteostasis to pathogenesis. *Biochim Biophys Acta Gen Subj* **1864**, 129338 (2020).

8. R. Flaumenhaft, B. Furie, Vascular thiol isomerases. *Blood* **128**, 893-901 (2016).

9. J. Chiu, P. J. Hogg, Allosteric disulfides: Sophisticated molecular structures enabling flexible protein regulation. *J Biol Chem* **294**, 2949-2960 (2019).

10. J. Ahamed *et al.*, Disulfide isomerization switches tissue factor from coagulation to cell signaling. *Proc Natl Acad Sci U S A* **103**, 13932-13937 (2006).

11. S. Kumar *et al.*, An allosteric redox switch in domain V of beta2-glycoprotein I controls membrane binding and anti-domain I autoantibody recognition. *J Biol Chem* **297**, 100890 (2021).

12. J. Cho *et al.*, Protein disulfide isomerase capture during thrombus formation in vivo depends on the presence of beta3 integrins. *Blood* **120**, 647-655 (2012).

13. J. Li *et al.*, Platelet Protein Disulfide Isomerase Promotes Glycoprotein Ibalpha-Mediated Platelet-Neutrophil Interactions Under Thromboinflammatory Conditions. *Circulation* **139**, 1300-1319 (2019).

14. S. Chakravarthi, C. E. Jessop, N. J. Bulleid, The role of glutathione in disulphide bond formation and endoplasmic-reticulum-generated oxidative stress. *EMBO Rep* **7**, 271-275 (2006).

15. G. Tian, S. Xiang, R. Noiva, W. J. Lennarz, H. Schindelin, The crystal structure of yeast protein disulfide isomerase suggests cooperativity between its active sites. *Cell* **124**, 61-73 (2006).

16. C. Wang *et al.*, Structural insights into the redox-regulated dynamic conformations of human protein disulfide isomerase. *Antioxid Redox Signal* **19**, 36-45 (2013).

17. L. Peng, M. I. Rasmussen, A. Chailyan, G. Houen, P. Hojrup, Probing the structure of human protein disulfide isomerase by chemical cross-linking combined with mass spectrometry. *J Proteomics* **108**, 1-16 (2014).

18. R. A. Romer *et al.*, The flexibility and dynamics of protein disulfide isomerase. *Proteins* **84**, 1776-1785 (2016).

19.    R. B. Freedman *et al.*, 'Something in the way she moves': The functional significance of flexibility in the multiple roles of protein disulfide isomerase (PDI). *Biochim Biophys Acta Proteins Proteom* **1865**, 1383-1394 (2017).

20.    M. Okumura *et al.*, Dynamic assembly of protein disulfide isomerase in catalysis of oxidative folding. *Nat Chem Biol* **15**, 499-509 (2019).

21.    E. I. Biterova *et al.*, The crystal structure of human microsomal triglyceride transfer protein. *Proc Natl Acad Sci U S A* **116**, 17251-17260 (2019).

22.    M. Chinnaraj *et al.*, Bioorthogonal Chemistry Enables Single-Molecule FRET Measurements of Catalytically Active Protein Disulfide Isomerase. *Chembiochem*, (2020).

23.    H. Sanabria *et al.*, Resolving dynamics and function of transient states in single enzyme molecules. *Nat Commun* **11**, 1231 (2020).

24.    V. Kudryavtsev *et al.*, Combining MFD and PIE for accurate single-pair Forster resonance energy transfer measurements. *Chemphyschem* **13**, 1060-1078 (2012).

25.    S. Kalinin, A. Valeri, M. Antonik, S. Felekyan, C. A. Seidel, Detection of structural dynamics by FRET: a photon distribution and fluorescence lifetime analysis of systems with multiple states. *J Phys Chem B* **114**, 7983-7995 (2010).

26.    C. Wang *et al.*, Human protein-disulfide isomerase is a redox-regulated chaperone activated by oxidation of domain a'. *J Biol Chem* **287**, 1139-1149 (2012).

27.    I. Grossman *et al.*, Single-molecule spectroscopy exposes hidden states in an enzymatic electron relay. *Nat Commun* **6**, 8624 (2015).

28.    J. J. Alston, A. Soranno, A. S. Holehouse, Integrating single-molecule spectroscopy and simulations for the study of intrinsically disordered proteins. *Methods*, (2021).

29.    I. V. Gopich, A. Szabo, Theory of the energy transfer efficiency and fluorescence lifetime distribution in single-molecule FRET. *Proc Natl Acad Sci U S A* **109**, 7747-7752 (2012).

30.    A. Barth *et al.*, Dynamic interactions of type I cohesin modules fine-tune the structure of the cellulosome of Clostridium thermocellum. *Proc Natl Acad Sci U S A* **115**, E11274-E11283 (2018).

31.    I. Grossman-Haham, G. Rosenblum, T. Namani, H. Hofmann, Slow domain reconfiguration causes power-law kinetics in a two-state enzyme. *Proc Natl Acad Sci U S A* **115**, 513-518 (2018).

32.    M. Okumura, K. Noi, K. Inaba, Visualization of structural dynamics of protein disulfide isomerase enzymes in catalysis of oxidative folding and reductive unfolding. *Curr Opin Struct Biol* **66**, 49-57 (2020).

33.    I. V. Gopich, A. Szabo, Single-molecule FRET with diffusion and conformational dynamics. *J Phys Chem B* **111**, 12925-12932 (2007).

34.    Y. Santoso, J. P. Torella, A. N. Kapanidis, Characterizing single-molecule FRET dynamics with probability distribution analysis. *Chemphyschem* **11**, 2209-2219 (2010).

35.    B. Hellenkamp *et al.*, Precision and accuracy of single-molecule FRET measurements-a multi-laboratory benchmark study. *Nat Methods* **15**, 669-676 (2018).

36.    S. Felekyan, S. Kalinin, H. Sanabria, A. Valeri, C. A. Seidel, Filtered FCS: species auto- and cross-correlation functions highlight binding and dynamics in biomolecules. *Chemphyschem* **13**, 1036-1053 (2012).

37. J. D. Stopa, K. M. Baker, S. P. Grover, R. Flaumenhaft, B. Furie, Kinetic-based trapping by intervening sequence variants of the active sites of protein-disulfide isomerase identifies platelet protein substrates. *J Biol Chem* **292**, 9063-9074 (2017).

38. B. G. Hoffstrom *et al.*, Inhibitors of protein disulfide isomerase suppress apoptosis induced by misfolded proteins. *Nat Chem Biol* **6**, 900-906 (2010).

39. K. S. Cole *et al.*, Characterization of an A-Site Selective Protein Disulfide Isomerase A1 Inhibitor. *Biochemistry* **57**, 2035-2043 (2018).

40. S. Xu *et al.*, Discovery of an orally active small-molecule irreversible inhibitor of protein disulfide isomerase for ovarian cancer treatment. *Proc Natl Acad Sci U S A* **109**, 16348-16353 (2012).

41. H. Mazal *et al.*, Tunable microsecond dynamics of an allosteric switch regulate the activity of a AAA+ disaggregation machine. *Nat Commun* **10**, 1438 (2019).

42. C. Wang *et al.*, Plasticity of human protein disulfide isomerase: evidence for mobility around the X-linker region and its functional significance. *J Biol Chem* **285**, 26788-26797 (2010).

43. L. J. Byrne *et al.*, Mapping of the ligand-binding site on the b' domain of human PDI: interaction with peptide ligands and the x-linker region. *Biochem J* **423**, 209-217 (2009).

44. R. H. Bekendam *et al.*, A substrate-driven allosteric switch that enhances PDI catalytic activity. *Nat Commun* **7**, 12579 (2016).

45. E. Ruben *et al.*, The J-elongated conformation of beta2-glycoprotein I predominates in solution: implications for our understanding of antiphospholipid syndrome. *J Biol Chem* **295**, 10794-10806 (2020).

46. N. Pozzi, D. Bystranowska, X. Zuo, E. Di Cera, Structural Architecture of Prothrombin in Solution Revealed by Single Molecule Spectroscopy. *J Biol Chem* **291**, 18107-18116 (2016).

47. A. N. Kapanidis *et al.*, Fluorescence-aided molecule sorting: analysis of structure and interactions by alternating-laser excitation of single molecules. *Proc Natl Acad Sci U S A* **101**, 8936-8941 (2004).

48. A. C. Ferreon, C. R. Moran, Y. Gambin, A. A. Deniz, Single-molecule fluorescence studies of intrinsically disordered proteins. *Methods Enzymol* **472**, 179-204 (2010).

49. W. Schrimpf, A. Barth, J. Hendrix, D. C. Lamb, PAM: A Framework for Integrated Analysis of Imaging, Single-Molecule, and Ensemble Fluorescence Data. *Biophys J* **114**, 1518-1528 (2018).

50. T. E. Tomov *et al.*, Disentangling subpopulations in single-molecule FRET and ALEX experiments with photon distribution analysis. *Biophys J* **102**, 1163-1173 (2012).

51. S. Kalinin *et al.*, A toolkit and benchmark study for FRET-restrained high-precision structural modeling. *Nat Methods* **9**, 1218-1225 (2012).

# Supplementary Materials

**Figure S1.** Structural and functional characterization of the FRET variants

**Figure S2.** 2D FRET efficiency vs Stoichiometry plot of reduced PDI 88/467 before cleanup

**Figure S3.** 2D FRET efficiency vs Stoichiometry plots of PDI 57/401, PDI 57/467, PDI 88/401 and PDI 88/467

**Figure S4**. Control experiments to characterize PDI 88/467

**Figure S5.** 2D FRET efficiency vs lifetime plots of PDI 57/401, PDI 57/467 and PDI 88/401.

**Figure S6.** PDA analysis of PDI 88/467

**Figure S7.** Analysis of static double-stranded DNA constructs

**Figure S8.** Reductase activity of the PDI 88/467 and active site mutants

**Figure S9.** 2D FRET efficiency vs lifetime plots of active site variants under non-reducing and reducing conditions
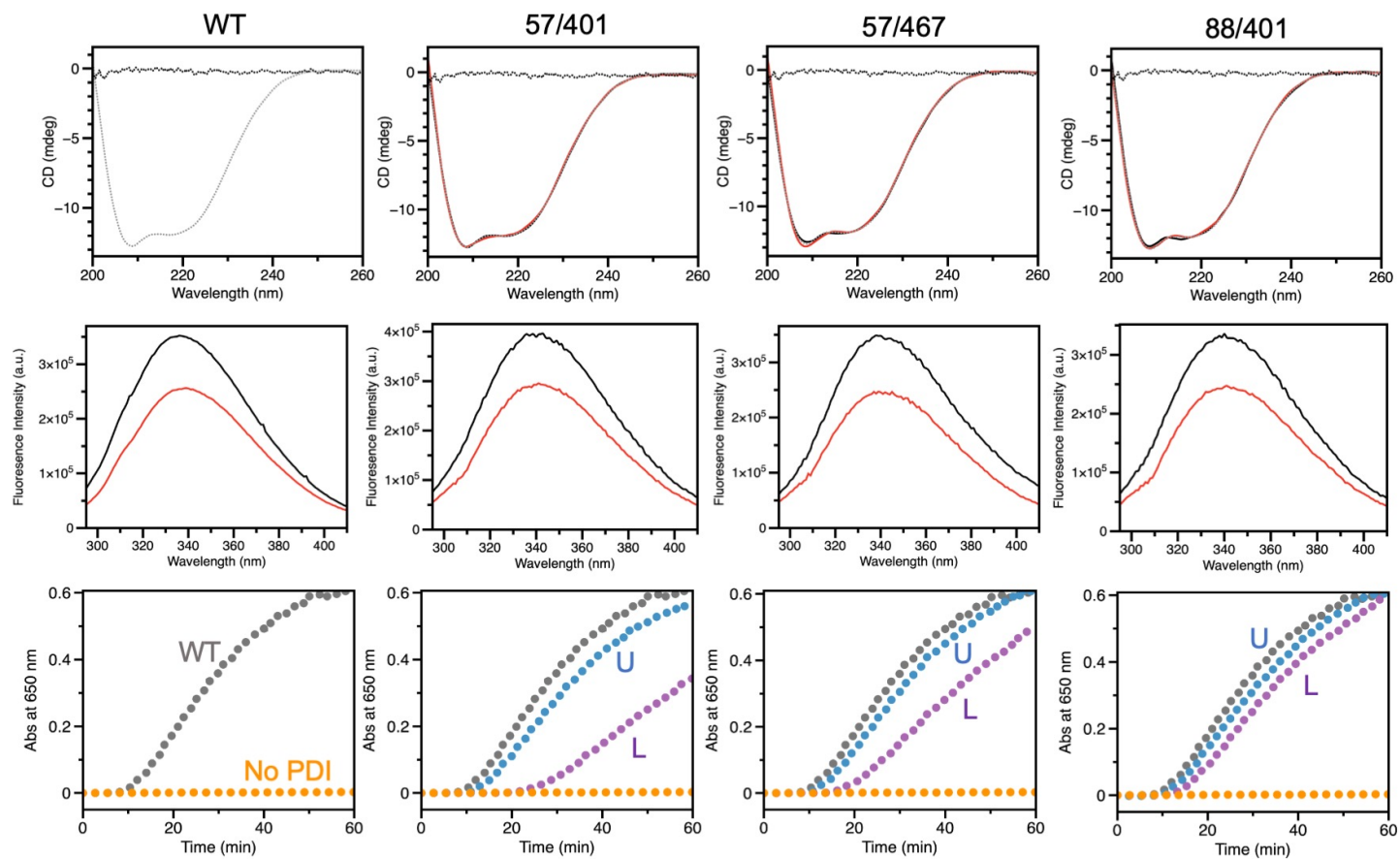
**Figure S1.** Structural and functional characterization of the FRET variants. Shown are far-UV CD spectra (top row), response to GSSG (red) and GSH (black) monitored by intrinsic fluorescence (center row) and progress curves for insulin reductase activity assay (bottom row) of PDI wild-type and variants. The labels U and L indicate unlabeled and doubly labeled protein samples, respectively. Results for the variant 88/467 are reported in **Figure 1** of the manuscript.
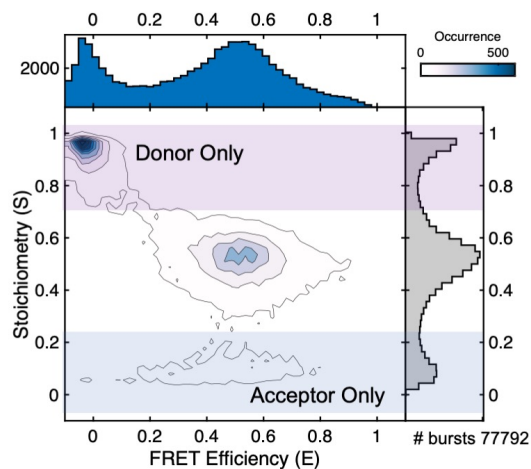
**Figure S2.** 2D FRET efficiency vs Stoichiometry plot of reduced PDI 88/467 before cleanup. Highlighted are Donor only (S>0.75, magenta) and Acceptor only (S<0.25, blue) populations. These species were discarded as they are not relevant to our analysis. On average, doubly labeled species account for 18-25% of the total.
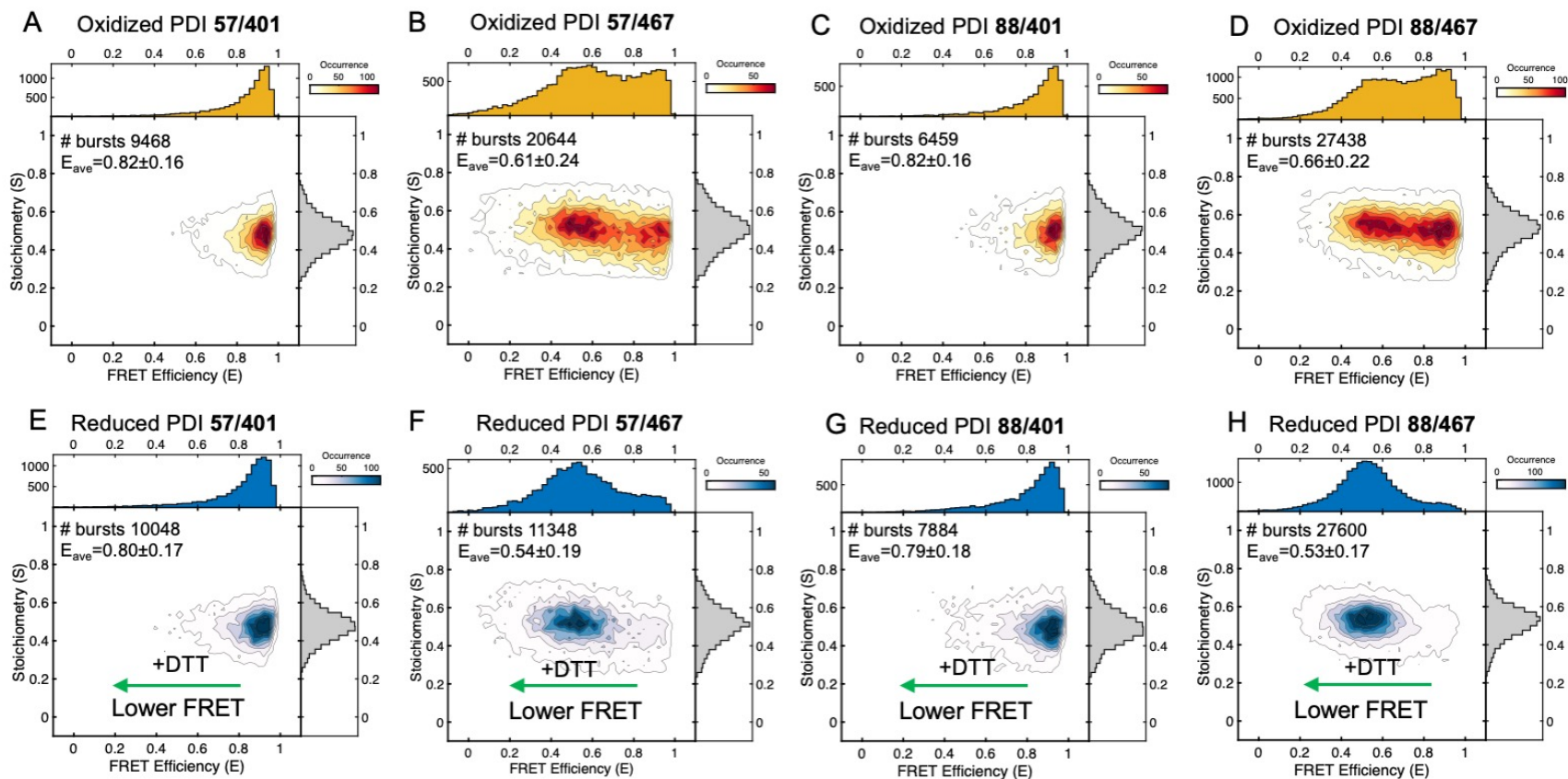
**Figure S3.** 2D FRET efficiency vs Stoichiometry plots of PDI 57/401, PDI 57/467, PDI 88/401 and PDI 88/467 under non-reducing (top, yellow) and reducing conditions (bottom, blue). Note how addition of DTT, while shifting $E_{ave}$ towards lower FRET, does not affect stoichiometry.
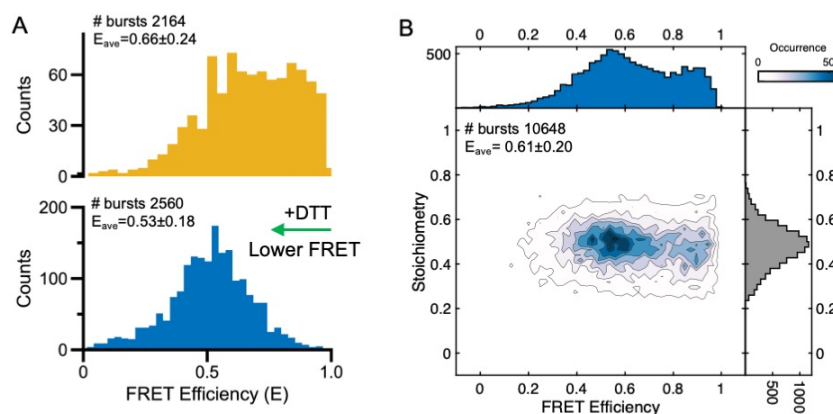
**Figure S4**. Control experiments to characterize PDI 88/467. **(A)** PDI 88/467 labeled with sulfo-Cy3/sulfo-Cy5 azide (Lumiprobe) under non reducing (top, yellow) and reducing (bottom, blue) conditions. PDI 88/467 labeled with Cy dyes displays similar high to low FRET transition in the presence of DTT compared to PDI 88/467 labeled with Atto dyes. **(B)** PDI 88/467 labeled with Atto dyes in the presence of 1 mM GSH. GSH is less potent than DTT when used at the same concentration.
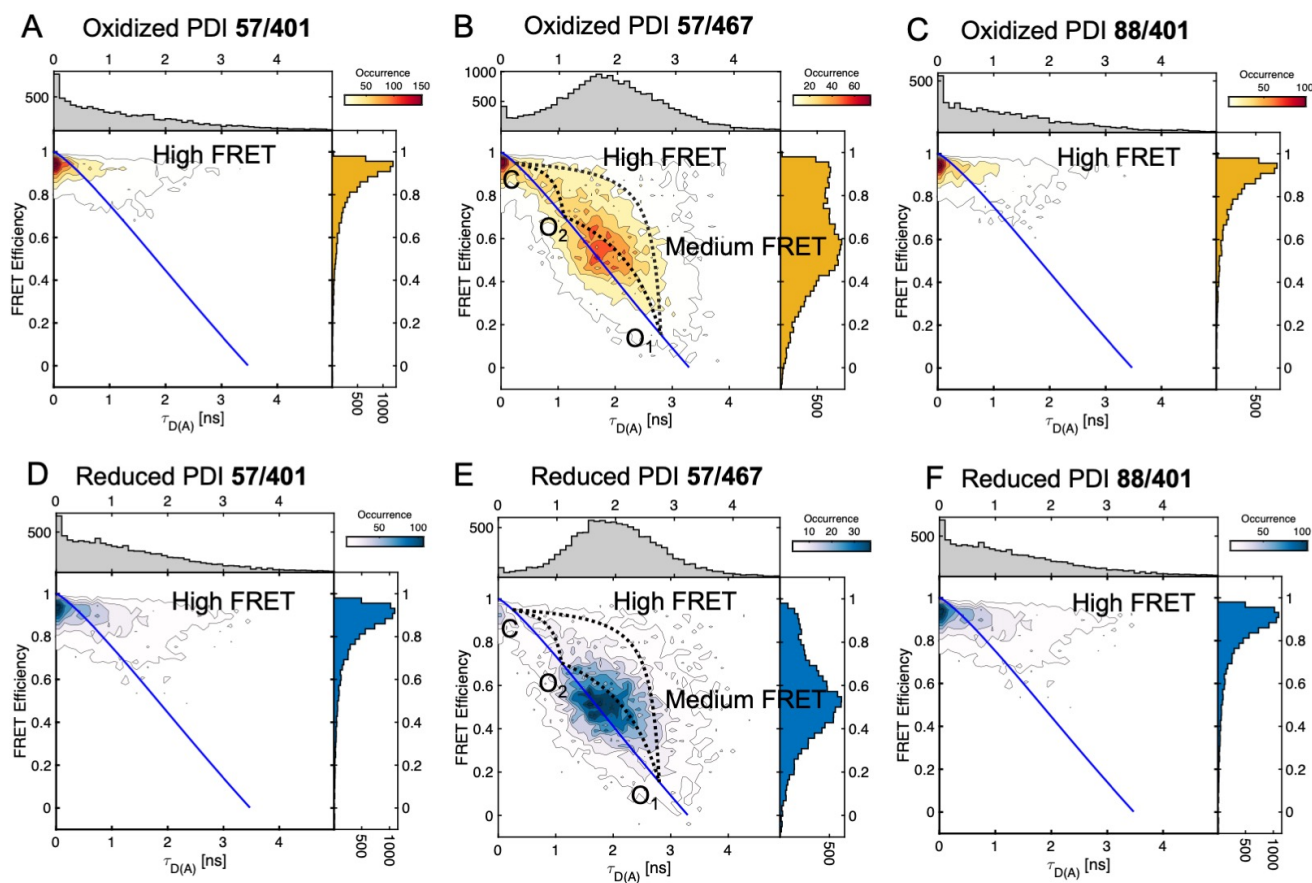
**Figure S5.** 2D FRET efficiency vs lifetime plots of PDI 57/401, PDI 57/467 and PDI 88/401 under non-reducing (top, yellow) and reducing (1 mM DTT) conditions (bottom, blue). Static FRET lines (solid blue lines) are shown in each plot. Due to high FRET, PDI 57/401 **(A** and **D)** and PDI 88/401 **(B** and **E)** show only a hint of dynamics, which manifests as a small but significant deviation of the high FRET ensemble towards the right of the static FRET line. Also evident in these plots is the shift toward lower FRET induced by DTT. PDI 57/467 **(C** and **F)**, in contrast to PDI 57/401 and PDI 88/401, but similar to PDI 88/467 (**Figure 3** of the main text), shows a very clear dynamic signature documenting dynamic exchange between closed (high FRET, C) and open (medium FRET, O) ensembles. These two ensembles are characterized by mean fluorescence lifetime values of ~0.25 and ~1.8 ns, respectively. The open ensemble of PDI 57/467, similar to PDI 88/467, is shifted toward the right of the static FRET line indicating fast dynamics between open states. Using the same methodology described in the main text, we identified $O_1$ (1.1±0.2 ns) and $O_2$ (2.8±0.3 ns), which are shown in the plot along the dynamic FRET lines (black dotted lines) that connect them.
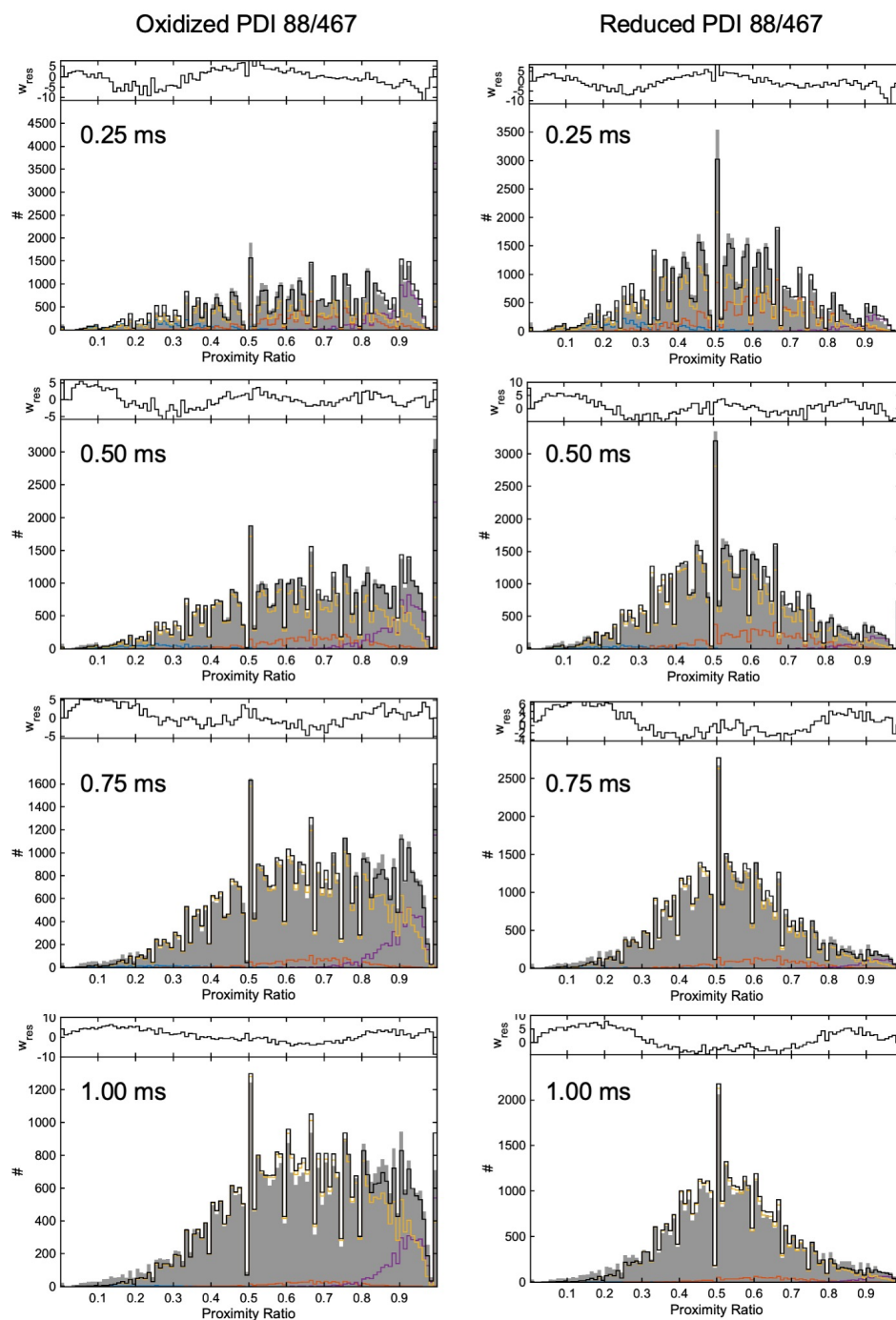
**Figure S6.** PDA analysis of PDI 88/467. PDA was performed on dataset binned at 0.25, 0.5, 0.75 and 1 ms. Photons from each burst were used to build a proximity ratio (PR) histogram. The resulting histogram was then fitted using a Monte Carlo approach for simulating the burst-wise histogram using a dynamic three-state model. To assess robustness of the fit, PDA was repeated by systematically varying the initial value of the rate constants to 1, 0.5 and 0.75 ms$^{-1}$ (min 0, max 10) while keeping the other settings identical. Corresponding weighted residuals are shown above each plot.
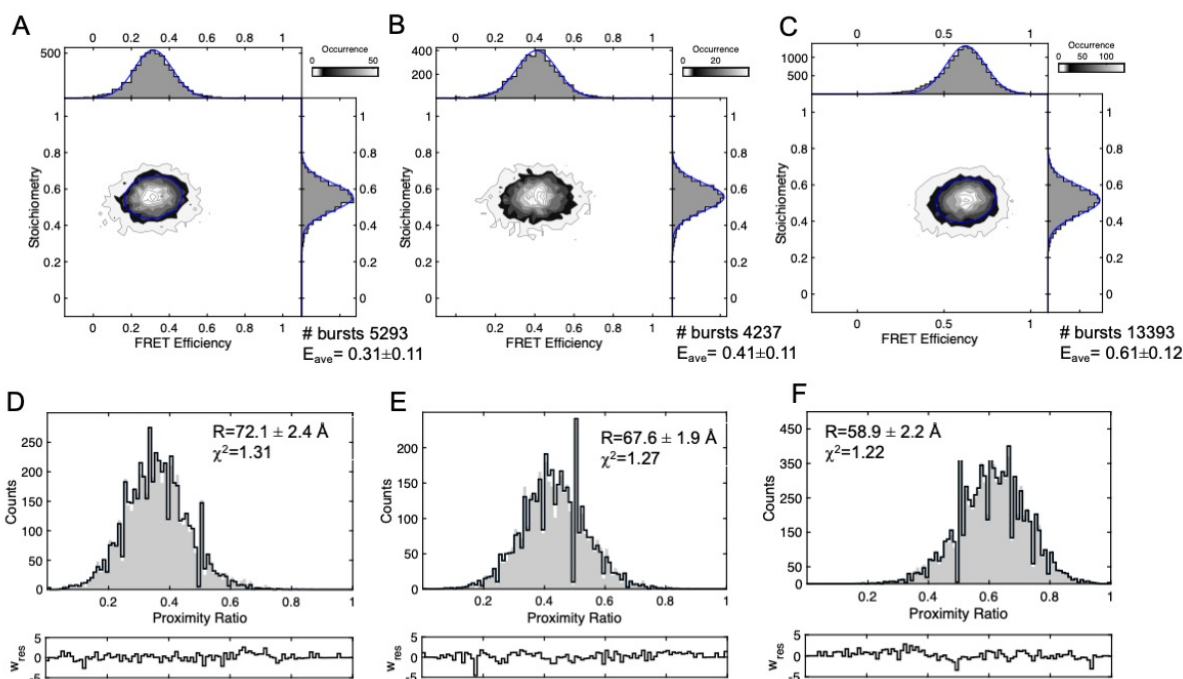
**Figure S7.** Analysis of static double-stranded DNA constructs. 2D plots **(A, B and C)** and PDA **(D, E and F)** analysis of DNA duplexes with probes separated by 19 **(A)**, 17 **(B)** and 14 **(C)** base pairs. Single-stranded DNA molecules were purchased (IDT Inc., Coralville, LA) and fluorescent dyes (Atto550/647N) were attached to amino dT residues obtained by substituting T to iAmMC6T. dsDNA molecules were formed by hybridization. Experimental conditions are 100 pM in TBS-Tween 0.01%. FRET histograms best fit to a one Gaussian distribution (blue). Note how the standard deviation for static species is significantly smaller compared to values obtained in this work for PDI **(Table 1)**, supporting the view that PDI adopts multiple conformations in solution. PDA was performed on dataset binned at 1 ms. Photons from each burst were used to build a proximity ratio histogram. The resulting histogram was then fitted using a Monte Carlo approach for simulating the burst-wise histogram using one Gaussian. Corresponding weighted residuals are shown below each plot.
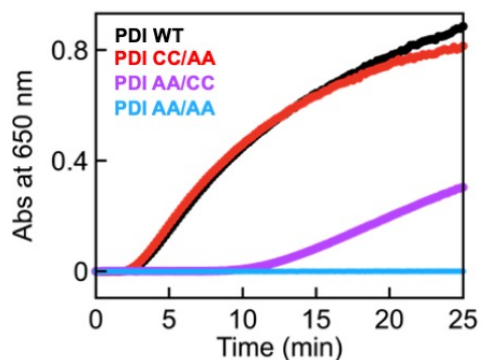
**Figure S8.** Reductase activity of the PDI 88/467 and active site mutants. Reductase activity of PDI 88/467 (WT, black) and active site variants PDI 88/467 C53A/C56A/C397AC400A (AA/AA, blue), PDI 88/467 C397AC400A (CC/AA, red) and PDI C53A/C56A (AA/CC, magenta) monitored by the insulin assay. Note how the catalytic activity of PDI CC/AA is similar to PDI WT but different from PDI AA/CC, whose catalytic activity is compromised. Among the two active sites, the one in the **a** domain is the most important for insulin reduction. PDI AA/AA is catalytically inactive, as expected, since no longer contains cysteine residues in the active sites.
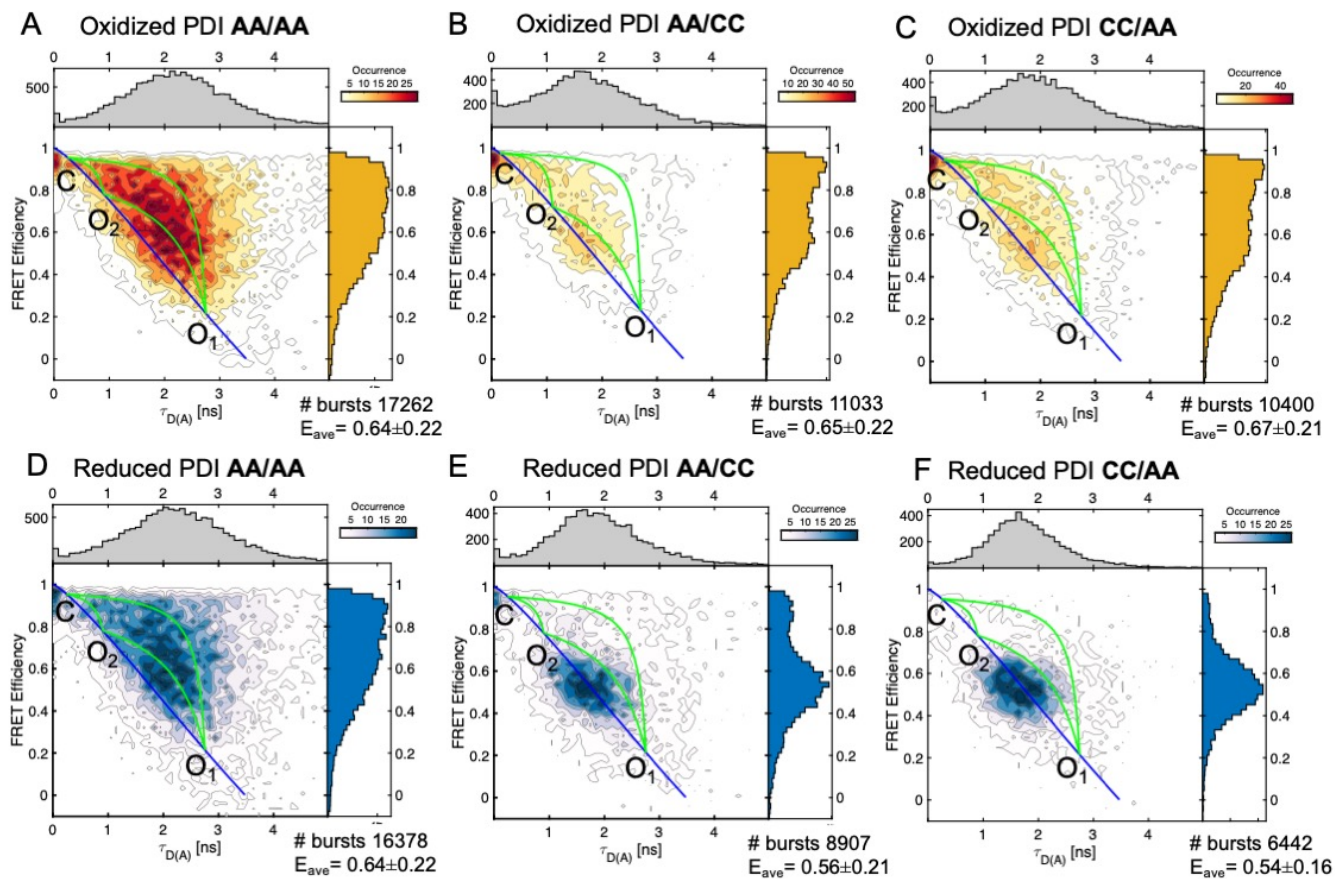
**Figure S9.** 2D FRET efficiency vs lifetime plots of active site variants under non-reducing (top, yellow) and reducing conditions (bottom, blue). Shown are static (solid blue lines) and dynamic (solid green lines) FRET lines connecting the FRET states. The lines were drawn as described in the main text. The position of C, $O_1$ and $O_2$ is indicated. The fraction of each population was obtained by PDA and is reported in **Table 4**.